Spatio-temporal variability of a chlorophyll-a based biomass index and influence of coastal sources of enrichment in the Algerian Basin

Romaissa Harid, Hervé Demarcq, Mehdia-Asma Keraghel, Malik Ait-Kaci, Mohamed Zerrouki, Nour-El-Islam Bachari, Fouzia Houma

Spatio-Temporal variability of a Chlorophyll-*a* based biomass index and influence of coastal sources of enrichment in the Algerian Basin

Romaissa Harid [a,b,*], Hervé Demarcq [b], Mehdia-Asma Keraghel [a], Malik Ait-Kaci [a], Mohamed Zerrouki [a], Nour-El-Islam Bachari [c], Fouzia Houma [a]

[a] ECOSYSMarL: Laboratoire des Écosystèmes Marins et Littoraux , École Nationale Supérieure des Sciences de la Mer et de l'Aménagement du Littoral (ENSSMAL), Campus Universitaire de Dely Ibrahim Bois des Cars, B.P. 19, 16320, Alger, Algeria

[b] MARBEC, IRD, Ifremer, CNRS, Univ Montpellier, Sète, Avenue Jean Monnet, CS 30171, 34203 Sète cedex, France

[c] USTHB : Université des Sciences et Technologie Houari Boumedien, Département Écologie et Environnement, BP 32 Bab Ezzouar, 16111 Alger, Algeria

The e-mail address and ORCID iD of each authors:

(r.harid@enssmal.dz, https://orcid.org/0000-0003-1418-7091), herve.demarcq@ird.fr, https://orcid.org/0000-0003-1995-1183), (ma.keraghel@enssmal.dz, https://orcid.org/0000-0002-5145-4913), (m.ait-kaci@enssmal.dz), (m.zerrouki@enssmal.dz, https://orcid.org/0000-0002-8842-9535), (n.bechari@usthb.dz, https://orcid.org/0000-0001-6686-2429), (f.houmabachari@enssmal.dz)

[*] **Corresponding author**: Romaissa Harid /r.harid@enssmal.dz/ romaissa.harid@hotmail.fr /+213 556 222 824

Highlights

- A specific fortnightly climatology of 1-km resolution Chlorophyll-*a* has been generated over the Algerian basin from MODIS data to explore the coastal domain.
- The Algerian Basin is characterised by two extreme seasons of high and low biomass, separated by sharp transitions, while the coastal area reveals a separated dynamic.
- Discontinuous and intense coastal cross-shore gradients reveal specific coastal sources of enrichments.
- A Chl-*a* based integrated index was defined to determine the importance of coastal enrichments.
- The Chl-*a* biomass in Algerian coastal waters is mainly associated with enrichments from wadis and cities with a pronounced seasonal effect.

Abstract. This study investigates the spatial distribution and temporal variability of chlorophyll-*a* (Chl-*a*) biomass in the Algerian Basin (AB) along its meridional and cross-shore dimensions, focusing on coastal enrichments. After correcting most atmospheric disturbances in the daily MODIS Level-2 data series between 2003 and 2018, a fortnightly climatology of 1-km resolution Chl-*a* has been generated to account for specific coastal features previously poorly evidenced from 4-km level-3 data. The AB is characterised by two extreme seasons of high and low biomass, separated by sharp transitions, that characterise the offshore domain. The coastal area (<10 km) reveals an intense and distinct dynamic associated with highly productive local hotspots rather than seasonal variability. A biomass index is proposed as the horizontally integrated Chl-*a* concentration from the coastline to the most offshore extension of the 0.5 mg m^{-3} Chl-*a* isopleth. This index separately quantifies the cumulative biomass of both offshore and coastal domains with large alongshore variability. Low values (<5 g m^{-2}) were observed in the offshore area during summer and high values during the spring blooms (up to 40 g m^{-2}), while

maximum values (>50 g m^{-2}) were locally observed in the coastal domain. The narrow coastal area alone represents 44% of the total biomass, with coastal hotspots where the enrichment is up to 5 times higher than offshore. Multivariate modelling of the potential factors favouring coastal enrichments shows that the phytoplanktonic biomass in coastal waters is mainly associated with enrichments from wadis and seasonally from city sewage as well as by the presence of a bay. A separate source of enrichment is undoubtedly associated with the presence of aquaculture cages.

Keywords: Ocean colour; alongshore variability; wadi; anthropic enrichment; MODIS.

1. Introduction

Chlorophyll-*a* (Chl-*a*) biomass is associated with the net primary production in marine ecosystems, and marine physical and biochemical processes strongly influence its variability. A precise description of the spatio-temporal variability of Chl-*a* biomass is necessary to understand coastal marine systems functioning. The Chl-*a* concentration in the southwestern Mediterranean Sea (Med) is closely related to winter mixing and summer stratification. The Med ecosystem is increasingly threatened by human activities in coastal areas, as well as by a continuing warming trend (Vargas-Yáñez et al., 2010). A recent study conducted by Keraghel et al. (2020) highlights that the southwestern Med is a net sink of carbon dioxide, even compared to the Med as a whole, which is a significant contributor at the global level (Khatiwala et al., 2013). Scientists are still trying to understand the evolution of the Med ecosystem to better assess current and future changes and consider solutions to mitigate some impacts of global warming.

The Algerian Basin (AB) is classified as mesotrophic (D'Ortenzio and Ribera d'Alcalà, 2009; Harid et al., 2018; O'Reilly and Werdell, 2019). Water exchange across Gibraltar has a significant influence on its general circulation (Béranger et al., 2005; Millot, 1989; Peliz et al., 2009) and controls its nutrient content (Bethoux et al., 2002; Crispi and Pacciaroni, 2009; Elbaz-Poulichet et al., 2001; Huertas et al., 2009), with a direct influence on the Chl-*a* based

phytoplanktonic biomass. In winter, the presence of distinct water bodies indicates the eastward movements of anticyclonic eddies (Olita et al., 2011), generated by instabilities in the Algerian current (Millot et al., 1990), which enrich the surface water and increase its primary production. The Atlantic water flow is characterised by a transit time of two to four months between Gibraltar and the Algerian coasts (Millot, 1999), strongly influencing the seasonal Chl-*a* signal (Salgado-Hernanz et al., 2019). In summer, the stability of water masses limits the nutrient input (Moutin and Prieur, 2012), leading to a decrease in phytoplankton production.

The continental shelf of the AB is very narrow (15 km on average) and is neglected in most studies. Nonetheless, the shelf is the richest domain of the AB and shelter more complex interactions than in the offshore domain. Ocean colour remote sensing has provided high-quality observations in this respect for over twenty years on the abundance and distribution of Chl-*a* concentration, which is considered a proxy for phytoplankton biomass (Cullen, 1982; Strickland, 1965). Turbid waters in the Med are rare compared to other seas (Morel et Prieur, 1977). According to Antoine et al. (1995), the coastal case-2 waters (where other constituents as mineral particles are also present) in the whole Med are estimated to be 5%. Currently, ocean colour analysis coupled with in-situ data could be used to characterise and monitor phytoplankton blooms (Barale et al., 2008; Cerino et al., 2019; Groom et al., 2019; Lavigne et al., 2015; Mayot et al., 2016; Palmiéri et al., 2018). In previous studies, a significant limitation was related to the poor representation of coastal patterns due to Level-3 data at 4-km resolution (as in Lavigne et al., (2015), Marañón et al., (2020), Mayot et al., (2016), Volpe, (2012), Volpe et al., (2018)).

To this end, our study proposes a practical approach to improve the quality of the standard MODIS-Aqua Level-2 1-km resolution (swatch) Chl-*a* product, specifically in coastal environments, where the higher data resolution provides more detailed information. A comparison between simultaneous in-situ and satellite Chl-*a* was performed to assess the

accuracy of MODIS Chl-*a* data in AB. In addition, a cumulative Chl-*a* biomass index (I_B) was developed to synthesise the spatial patterns and variability of Chl-*a*. This paper describes the seasonal climatology of I_B in AB from 16 years of data (2003-2018), focusing on offshore and coastal areas separately. Finally, a discussion on the influence of different sources of coastal enrichment on the Chl-*a* biomass in the AB is presented.

2. Methods

2.1 Study area

The Algerian Basin (Fig. 1) is a major energetic area for mesoscale activity throughout the Med (Amores et al., 2013; Pessini et al., 2018). Millot and Taupier-Letage (2005) described the East flowing Algerian current, which carries Atlantic surface water, is 50-100 km wide and 100-200 m thick with a speed of some 10s cm s^{-1} (El-Geziry and Bryden, 2010). It generally follows the continental slope and generates small eddies of 10-100 km diameter, lasting a few weeks or months. Periodically, this current forms a growing meander of 50-100 km; it can detach to form an anticyclonic eddy of 100-200 km diameter that encompasses the entire thickness of the Med water (El-Geziry and Bryden, 2010; Fani et al., 2014; Millot, 1989). Some oceanic eddies persist for up to three years, circulating in the AB in a cyclonic circuit (Millot and Taupier-Letage, 2005). Thus, the AB acts as a reservoir where Atlantic waters accumulate before flowing either eastwards (surface waters) or northwards (deep waters) of the Med (Millot, 1999). Indeed, this buffer zone decouples the inflow and outflow of Med surface waters.

2.2 Satellite data sources

We used daily Level-2 Chl-*a* concentration data from the MODIS-Aqua sensor from 2003 to 2018 at 1-km nominal resolution. The data set consists of 5844 daily observations from 15020 individual orbits acquired from NASA's Ocean Color website (NASA's Ocean Color Web, 2019). Each daily data field was remapped over the AB, between 35°N-40°N and 6°W-10°E (Fig. 1), at

120 a spatial resolution of 96 pixels per degree of latitude and longitude. The equivalent daily
121 MODIS Level-3 mapped data set at 4-km spatial resolution was obtained from the NASA Ocean
122 Data Processing System. This data set was compared to the MODIS Level-2 data set to
123 demonstrate permanent coastal Chl-*a* patterns. The climatological period from 1 to 15 January
124 2003-2018 (Fig. 2) illustrates the differences between both spatial resolutions of 1-km and 4-km.
125 In this work, a corrected version of the MODIS Level-2 data at 1-km was used to adequately
126 describe the AB Chl-*a* variability in the coastal and offshore areas.

127 **2.3 Cloud masking improvement of MODIS Level-2 Chl-*a* data**

128 This section describes the specific processing steps applied for the first time to the standard
129 cloud-corrected Level-2 Chl-*a* fields to detect and remove spurious patterns that affect data
130 quality, even in fortnightly averages (Fig. 2b). Specifically, we noticed the presence of (i)
131 partially cloudy pixels at the edge of the cloud mask, resulting in spurious high Chl-*a* values and
132 (ii) noisy pixels. Three criteria were used to discriminate these contaminated pixels: 1) a
133 maximum allowable value associated with a realistic Local Chl-*a* Gradient (LG), 2) a maximum
134 value of daily Chl-*a* change during 3-day periods (Temporal Variation, "TV"), and 3) their
135 position as Isolated Pixels (IP) inside the cloud mask. The pixel values corresponding to any of
136 these criteria cited here are selected and replaced by the missing value.

137 *2.3.1 Local Gradient (LG) criteria*

138 First, we applied a 3x3 Gaussian filter (Eq. 1) followed by a Sobel Gradient filter (Sobel, 1990)
139 as follows:

140 $$k(x,y) = \frac{1}{2\pi\sigma^2} exp\frac{-(x^2+y^2)}{2\pi^2} \quad (1)$$

141 where, k(x,y) is the matrix of the kernel used to convolute the original image; *x* and *y* are the
142 pixel's position along the abscissa and ordinate axes respectively.$\sigma^2$is the variance of the 3x3
143 pixel matrix.

144 The horizontal and vertical components of the Sobel gradient (Eq. 2 and Eq. 3, respectively)
145 were separately computed and combined into the final gradient (Eq. 4):

146 $$G_h[x][y] = k(x,y) * \begin{Bmatrix} -1 & -2 & -1 \\ 0 & 0 & 0 \\ 1 & 2 & 1 \end{Bmatrix} \quad (2)$$

147 $$G_v[x][y] = k(x,y) * \begin{Bmatrix} -1 & 0 & 1 \\ -2 & 0 & 2 \\ -1 & 0 & 1 \end{Bmatrix} \quad (3)$$

148 $$Sobel_G\,[x][y] = \sqrt{G_h^2[x][y] + G_v^2[x][y]} \quad (4)$$

149 As spurious gradients are mainly associated with atmospheric perturbations in the vicinity of
150 clouds, a maximum threshold value of the local Sobel gradient of Chl-*a* was considered to detect
151 outlier pixels (Fig. 3a), at a maximum distance of 5 km from cloud borders (black areas in Fig.
152 3b). After several tests, two thresholds were defined: 0.4 mg m^{-3} km^{-1} and 1 mg m^{-3} km^{-1}
153 respectively for the coastal zone (distance from the coast <5 km) (Fig. 3c) and the offshore area.

154 *2.3.2 Temporal Variability (TV) criteria*

155 Each daily individual Chl-*a* pixel value of a given day (Day_0) was compared to the average value
156 of the previous day (Day_{-1}) and the following day (Day_{+1}) when one or both values are available
157 to detect anomalous Chl-*a* variations through time, as given by Eq. 5:

158 $$TV = Day_0 - \left(\frac{Day_{-1}+Day_{+1}}{2}\right) \quad (5)$$

159 This difference was then compared with the maximum threshold of temporal variability set at 2
160 mg m^{-3}. Furthermore, this test was applied in the offshore domain only (distance from coast >20
161 km) to consider the higher spatio-temporal variability of the coastal environment (Fig. 3e).

162 *2.3.3 Isolated Pixel (IP) removal*

163 This criterion is used to eliminate pixels closely associated with a cloud structure. We considered
164 that Chl-*a* pixels bordered by more than five cloudy pixels (including those isolated in a cloud)

belong to the same atmospheric structure and should be eliminated (Fig. 3f).

2.3.4 Combination of criteria

The three criteria mentioned above were cumulated, and the pixels marked by at least one criterion were removed. The resulting daily data are significantly less noisy, as shown in Fig. 3h. A fortnightly climatology of Chl-*a* at 1-km resolution is then computed for the whole AB.

2.4 Comparison between in-situ and satellite Chl-*a* data

We compared the resulting 1-km satellite Chl-*a* data with an initial set of 70 high-performance liquid chromatography (HPLC) measurements of surface Chl-*a* concentration obtained during the SOMBA (*Système d'Observation à la Mer dans le Bassin Algérien*) cruise in the AB between August 13 and September 10, 2014 (Mortier et al., 2014). Further details about the cruise are available at https://doi.org/10.17600/14007500. Calibration precision was estimated to be 0.4% from the HPLC 1200 instrument used for the Chl-*a* measurements. A total of 34 measurements were retained according to their correspondence with satellite passes within ± 6 hours. The nearest pixel at 1-km resolution was considered. A representativity error (RE) was also considered, based on the proximity of a high Chl-*a* gradient, which we defined at a value of 0.01 mg m^{-3} km^{-1}, compared with the effective Chl-*a* gradient measured in a 5x5 pixel matrix (Error bars in Fig. 4). In contrast, this spatial variability is generally low for pixels far from eddies (Fig. 4b and 4e). We also checked the proximity of the HPLC measurements to the clouds (less than 5 km); only two measurements deviate from this criterion (Fig. 4c and 4d).

2.5 Biomass index

A modified version of the coastal Chl-*a*-based index developed by Demarcq et al., (2007) was applied. Based on the Chl-*a* concentrations, a threshold (β) of Chl-*a* concentration was set to compute the proposed integrated Chl-*a* biomass index (I_B) in AB. This threshold was chosen as a value observed during all seasons (Fig. 7b). A value of 0.5 mg m^{-3} was selected according to this

criterion for the present study. The integrated Chl-*a* biomass index was calculated at each coastal point with the following formula:

$$I_B = \left(\sum_{dist=\mathrm{Dist}_{min}}^{Dist_{(\beta,max)}} \overline{Chla}\right) \times Dist_{(\beta,max)} \quad (6)$$

where, the average Chl-*a* is calculated by the formula:

$$\overline{Chla} = \left(\sum_{i=1}^{n_{(\beta,max)}} Chla\right) / n_{(\beta,max)} \quad (7)$$

where, $n_{(\beta,max)}$ is the position of the most distant pixel of the cross-shore transect.

The cross-shore distance associated with the index $Dist_{(\beta,\,max)}$ is the most distant position where Chl-*a* ≥ β with the constraint $Dist_{(\beta,\,max)} \leq max$, is the maximum allowable distance. When this distance is determined, all pixel values from $Dist_{\min}$ to $Dist_{(\beta,\max)}$ are considered, regardless of their value; sometimes slightly <β. If no data ≥β was found within a profile, the computation of I_B was performed only for the first valid pixel at the only $Dist_{\min}$ position, regardless of its value. The maximum distance for $Dist_{(\beta,\,max)}$ in km was chosen at 10 km for the coastal area and 80 km for the next offshore area, according to the average structure of the cross-profiles (Fig. 6b). It is important to note that for continuity reasons, the first (inner) pixel of the offshore area was considered the pixel immediately offshore of the last of the coastal areas. The integrated coastal and offshore biomass indices were then calculated for the entire Algerian coastline or part of it (Table 1).

To estimate the relationships between Chl-*a* biomass (Chl-*a* or I_B) classes and factor variables representative of the different sources of coastal enrichment, we applied the Generalized Linear Model (GLM) approach. All data analysis was done using the "stats" package version 3.4.4 of the R software.

2.6 Physical oceanographic data

2.6.1 Altimetry data

Geostrophic ocean currents and total kinetic energy (TKE) were extracted from the CMEMS

(Copernicus Marine Environmental Service) database of the *SEA-LEVEL GLO PHY L4 REP OBSERVATIONS 008 047* altimetry data product (http://marine.copernicus.eu, last accessed February 27, 2019), for the same period, and remapped in the AB at a spatial resolution of 0.25° (Fig. 1 for geostrophic currents and Fig. S2b for TKE).

2.6.2 Mixed Layer Depth

The mixed layer depth (MLD) has been defined in previous studies (as Lavigne et al., (2015) and Volpe, (2012)) using in-situ data in the Med (AB included). In this study, the monthly climatology (1969 to 2013) of the MLD was used as defined by Houpert et al. (2015) (data from https://www.seanoe.org/data/00354/46532/).

2.6.3 Wadis outflows

Outflow data measured by the Algerian National Agency for Hydraulic Resources (*Agence Nationale des Ressources Hydrauliques*, ANRH, http://www.anrh.dz/) were used to evaluate the possible influence of wadis (temporary rivers) on the Chl-*a* variability along the Algerian shelf.

3. Results

We show that a high-resolution fortnightly climatology very significantly improves the description of the spatio-temporal variability of Chl-*a* (including abrupt seasonal changes) and a spatio-temporal view of the enrichment sources. We explore here the coastal and offshore domains along meridional and cross-shore transects, focusing on the coastal domain, to understand the main seasonal dynamics of these enrichments.

3.1 Impact of data resolution on the description of seasonal patterns

Firstly, we compared the standard (original) MODIS data (1-km) to the corrected (this work) MODIS data (1-km). The improvement is particularly high during winter (characterised by a large cloud cover) with better detection of atmospherically contaminated pixels (Fig. 5). An example of the impact of Chl-*a* outlier values in the spatial distribution of the time series averages is represented in Fig. 5a and Fig. 5b for a fortnightly, and in Fig. 5c and Fig. 5d for a monthly climatological average. This correction produces a moderate decrease in Chl-*a* mainly

239 during the productive season, reinforcing the descripting cross-shore profile. The resulting
240 fortnightly climatology of MODIS Level-2 Chl-*a* data (at 1-km resolution) in the AB can be
241 found online at https://doi.org/10.5281/zenodo.5390383 .

242 The new fortnightly climatology at 1-km resolution was compared to the 4-km resolution used in
243 all previous studies. Seasonal variability of Chl-*a* from the corrected MODIS 1-km Level 2 data
244 (Fig. 6b) was explored along average cross-shore transects and compared to the MODIS 4-km
245 Level-3 data (Fig. 6a). A closer look at the shorter distances (0-10 km) (Fig. 6c and 6d) shows
246 that, as expected, the improvement is very significant and highlights much stronger cross-shore
247 patterns (Fig. 6e and 6f for the most contrasted months of March and August), both in terms of
248 Chl-*a* concentration average and seasonal patterns. The coastal Chl-*a* (0-10 km) from the 1-km
249 data is 37% higher than that from 4-km data (49% and 46% respectively at distances of 2 and 4-
250 km from the coast). The 4-km product cannot detect a significant part of the coastal enrichment,
251 representing 44% of the production of the AB from 1-km data, while only 25% are detected from
252 4-km data. Consequently, the spatial resolution impacts the scale of the description and more
253 importantly the high contribution of the coastal area in the regional marine productivity.

254 **3.2 MODIS Level-2 data validation in the AB**

255 The in-situ Chl-*a* data range between 0.062 and 0.307 mg m^{-3} (Fig. 4). These values are typical
256 for the AB offshore area during the oligotrophic season in the surface layer. Both sources of Chl-
257 *a* data span nearly the same magnitude. The HPLC data have a slightly lower mean and median
258 (respectively 0.100 mg m^{-3} and 0.094 mg m^{-3}) than the satellite data (0.105 mg m^{-3} and 0.104 mg
259 m^{-3}). It should be noted that the satellite has a vertically integrating effect (exponentially
260 decreasing) on the estimated Chl-*a* value. In contrast, the in-situ measurements represent
261 exclusively punctual surface values at 1 m depth and the remaining ones at 2 m depth. The final
262 error associated with the Chl-*a* satellite data was estimated at 0.025 (8% of the average) by the
263 RMSD (Root Mean Square Deviation) between Chl-*a* HPLC and MODIS Level-2 data.

No in-situ measurements were available in the coastal areas of the AB. Nevertheless, Pieri et al., (2015) have found that the OC3M standard algorithm (used in our work) gives valid results in the Western Mediterranean Sea when the Chl-*a* concentration does not exceed 1 mg m^{-3}. In our case, the Chl-*a* exceeds 1 mg m^{-3} generally in the three first kilometers from coast (i.e. the 3 first pixels) and only during the high production season (December to March, as shown in Fig. 6 and 7). To estimate the importance of the likely overestimation of the values >1 mg m^{-3}, we apply an empirical correction model with two levels of intensity, by reducing the values >1 mg m^{-3} by a factor of two and by a factor of three. The results show a relatively modest overestimation of respectively 6% and 9% of the Chl-*a* in these two extreme cases. This allows us to assume that a likely overestimation of the Chl-*a* values in the very coastal area does not significantly impact our conclusions.

3.3 Cross-shore and seasonal variability of Chl-*a*

Chl-*a* cross-shore sections (Fig. 6b) indicate that the lowest Chl-*a* concentrations are observed from May to October at all locations, both in coastal and offshore areas. The highest Chl-*a* concentrations, representing the productive season, are observed from November to April. In the coastal area, the maximum Chl-*a* can exceed 2 mg m^{-3} in winter (Fig. 7a) and 0.5 mg m^{-3} in summer (Fig. 7a). However, in the offshore area, beyond 10 km from the coast, the average minimum reach 0.5 mg m^{-3} in winter and 0.2 mg m^{-3} in summer (Fig. 6b and Fig. 7b). Beyond 10 km, the Chl-*a* concentration becomes stable during all seasons (Fig. 6b and Fig. 7a). Indeed, we chose the distance of 10 km from the coast as the shortest distance at which Chl-*a* seasonality becomes weak and stops increasing towards the offshore (Fig. 6b and 7b).

The cross-shore gradient is well pronounced throughout the year and increases exponentially towards the coast (Fig. 6b). The intensity of this gradient is maximum during the productive season and is always maximal at the coast and regularly decreases with increasing distance from the coast (Fig. 6b), ranging from 0.2 to 2 mg m^{-3} onshore (Fig. 6b) and 0.1 to 0.5 mg m^{-3} offshore

289 (Fig. 6b).

290 **3.4 Meridian variability and seasonality of Chl-*a* biomass index**

291 The integrated cross-shore biomass index (Section 2.6) was computed from each coastal point
292 northwards to integrate the Chl-*a* concentration up to a variable distance (Fig. 8b) where Chl-*a*
293 drops below the predefined value of 0.5 mg m^{-3} (see methods). The aim was to explore and
294 quantify the integrated coastal Chl-*a* biomass along the Algerian coastline (Fig. 8d). The value
295 was carefully chosen as the best threshold β = 0.5 mg m^{-3} that intersects the different average
296 cross-shore climatological profiles over the year (Fig. 7b). The red line in Fig. 8a represents the
297 maximum distance effectively reached during the productive season (we considered Chl-*a* <0.5
298 mg m^{-3} as oligotrophic and does not represent an enrichment). The resulting distance (Fig. 8b)
299 shows that the productive area varies over time from a few kilometres in summer (cyan area in
300 Fig. 8b) with a minimum of 1 km (when only one sea pixel is considered) to a maximum of 80
301 km in winter, mainly reached near the Alboran Sea in the west. The longitudinal gradient along
302 the coastline shows an apparent decrease of this distance eastward, which is well in line with the
303 decreasing influence of the enrichment of Atlantic waters entering the Alboran Sea and moving
304 eastwards.

305 The average Chl-*a* along the same transect (Fig. 8c) shows extreme variability between regions,
306 from values <0.5 mg m^{-3} in summer (this is possible when a minimum of one sea pixel is
307 considered) to values >2 mg m^{-3} between April and November, i.e., during low-biomass season.
308 The resulting biomass index I_B (Fig. 8d) is defined as the product of the previous distance by the
309 average Chl-*a* concentration along the same transect (Eq. 6). This index represents the spatial
310 integration of the most elevated Chl-*a* values along the cross-shore transect, while the vertical
311 dimension is partially considered by the attenuation depth of the satellite measurement.
312 Nevertheless, this depth represents a variable fraction of the euphotic layer, according to the
313 shape of the vertical Chl-*a* profile.

The Chl-*a* (Fig. 8c) represents a proxy of the average phytoplankton biomass over the cross-shore profile, while the spatially integrated index (I_B, Fig. 8d) is predominantly determined by the length of the profile (Fig 8b). The I_B index is expressed in g m^{-2} and varies between 20 and 50 g m^{-2} during the productive season (Fig. 8d) with a regular eastward decrease. Several peaks in phytoplanktonic biomass are observed (I_B is >45 g m^{-2}; between 2.2°W and 0.5°E from January to March, between 5.1°E to 5.5°E in January and February, and at 7.7°E from January to March-April). These peaks correspond to pronounced extensions of $Dist_{0.5mg}$ (Fig. 8b) as near the Alboran region or mostly to higher Chl-*a* values in the central and eastern parts of the AB (Fig. 8c). I_B is <10 g m^{-2} everywhere during the low-biomass season, except in the Algiers and Annaba bays (Fig. 8d). I_B is, in fact, practically zero from June to September in many locations where the Chl-*a* concentration barely exceeds 0.5 mg m^{-3} (Fig. 8c).

4. Discussion

The construction of a data set at 1-km spatial resolution allows investigating and extracting the specific enrichments of coastal origin, distinguishable from the large-scale seasonal cycle. Previous descriptions of the climatological cycle in the AB were based on monthly averages (instead of fortnightly in this study) and at a much higher spatial resolution. Therefore, our description of the cross-shore gradient of Chl-*a* and its variability along a longitudinal gradient becomes much more realistic and highlights the high importance of the coastal domain (<10 km) in the whole basin.

4.1 Processes governing Chl-*a* variability in AB

4.1.1 Seasonal variability

AB is characterised by two contrasting seasons (Fig. 7a): an early 3.5-month high-biomass season (mid-December to March) and a 4.5-month low-biomass season (June to mid-October), characterised by intense stratification. The two seasons are separated by quasi symmetrical and sharp 2-month transition periods in spring and autumn (Fig. 7a). The extreme precocity of the

339 productive period (between October and November), i.e. during a low sun elevation, clearly
340 shows that light is not the main limiting factor in the occurrence of winter blooms. The
341 seasonality of Chl-*a* is closely related to the dynamics of the Mixed Layer Depth (MLD, Fig. 7a,
342 brown line and Fig. S1 in supplementary material), which is maximum (40 m to 60 m) in winter
343 between December and February and very low (15 m) in summer from June to September.

344 It is well known that winter and spring blooms in the region are almost exclusively driven by the
345 nutrient input following autumn and winter vertical mixing (Fani et al., 2014; Huertas et al.,
346 2012; Lazzari et al., 2012; Millot et al., 1990; Pasqueron de Fommervault et al., 2015), as
347 reflected by our biomass index (Fig. 8d). Moreover, the results show that high Chl-*a* values
348 dominate several well-defined coastal areas outside the productive season, from April to
349 November (Fig. 8c). On a large scale, the variability of Chl-*a* concentration in the AB is known
350 to be driven by the inflow of nutrient-rich Atlantic waters that enter the Alboran Sea through the
351 Gibraltar strait (Taupier-Letage and Millot, 1988) and progress eastwards along the AB. The
352 same conclusions have also been drawn more recently by several authors (Fani et al., 2014;
353 Huertas et al., 2012; Lazzari et al., 2012; Pasqueron de Fommervault et al., 2015). Consequently,
354 the eastward propagating eddies modulate the circulation of water masses beyond the continental
355 shelf (Pessini et al., 2020), generating intense vertical mixing (Millot et al., 1990). Its positive
356 influence on productivity is perceptible up to the eastern part of the country and is reinforced by
357 nutrient enrichments from the bottom (Millot et al., 1990). The offshore vertical mixing is
358 considered to be the main factor influencing winter-spring enrichments before the summer-
359 autumn stratification period.

360 In addition to these two well-known potential sources of enrichment, we identified a third coastal
361 source: the presence of nutrients of coastal origin, generally associated with bays or gulfs, which
362 enhance local phytoplankton growth. The integrated Chl-*a* biomass index (I_B, Fig. 8d) is used in
363 this study as a proxy for the primary production dynamic in the AB. Better than local Chl-*a*

364 averages, it adequately describes the longitudinal variability of spring blooms due to its cross-
365 shore integrative capability. In other words, the Chl-*a* averages (Fig. 8c) gives a clear view of the
366 origin of the enrichment effects without considering their spatial importance. In contrast, the I_B
367 (Fig. 8d) integrates both components.

368 However, this index in Fig. 8d (and the associated average Chl-*a*) does not distinguish between
369 coastal and offshore sources of enrichment. We, therefore, divided it into an inshore and an
370 offshore component, as detailed in Section 2.6. The coastal area is defined as the distance
371 between the coast and the 0.5 mg m^{-3} isopleth position, with a maximum distance of 10 km (Fig.
372 6b). The offshore component is then defined as the area beyond this variable spatial limit up to a
373 maximum distance of 80 km. The maximum 10 km limit was chosen to best separate the coastal
374 and offshore signals, from the Chl-*a* signature (Fig. 9a-b) and the corresponding integrated
375 biomass index (Fig. 9c-d).

376 *4.1.2 Coastal enrichment*

377 Beyond the spatially averaged seasonal signal computed in both domains (Fig. 7a), the results
378 give precise insights about their regional alongshore variability, which is well distinguished by
379 the biomass index (Fig. 9c-d). The coastal biomass index (I_B, Fig. 9c) highlights the increase in
380 the duration of the productive season varies, that from 4 to 6 months from East to West and from
381 4 to 8 months (and more) in the coastal areas in the form of spatially distinct peaks of values >20
382 g m^{-2}. Some locations, such as the Algiers Bay (3.2°E) and the Annaba Bay (7.9°E), show high
383 index values almost yearly. In contrast, no Chl-*a* peaks are visible in the offshore area (Fig. 9d),
384 even in the locations where the highest coastal peaks are observed (Fig. 9c). The offshore area
385 exhibits a much more homogeneous spatial pattern with high cumulated biomass during the
386 central part of the productive season, with a maximum between January and February, except
387 near the Alboran Sea, where the maximum occurs one month later. The duration of the
388 productive season considering the I_B at 10 g m^{-2} limit, varies from 5 months (December to April)

389 west of 1°E with maximum values constantly between 30 g m^{-2} and 40 g m^{-2}, then is 4 months in
390 most of the area up to 7°E, to a minimum duration <2 months (mid-January to February) with
391 maximum values <25 g m^{-2}. Between 5°E and 6°E longitude, a distinct offshore maximum in the
392 biomass index (Fig. 9d and Fig. 11, blue curve) is observed during the productive season. This
393 feature probably corresponds to the relative permanence of the mesoscale cyclonic EAG (Eastern
394 Algerian Gyre, Fig. 1) as described by Testor et al., (2005) and where high Chl-*a* concentrations
395 are regularly found (Taupier-Letage, 2003).

396 The same processing was applied to compare these results with the equivalent information from
397 the 4-km Level 3 data and presented in Supplementary Fig. S2. As previously shown, the coastal
398 fraction of the enrichment is here only 25% (44% from 1-km data), and only two areas with Chl-
399 *a* peaks would be partially detected, regardless of the season. This clearly shows that 1-km data
400 are a minimum requirement to adequately explore the relative importance of the different sources
401 of enrichment in the coastal regions.

402 Coastal and offshore averages of the biomass index were calculated for all areas where high
403 biomass index values were observed, hereafter referred to as **H**igh-**B**iomass **C**oastal Zones (or
404 HBC), and outside these zones referred to as **L**ow-**B**iomass **C**oastal Zones (or LBC). The aim is
405 to separate the specific effects of local (coastal) enrichments from the large-scale enrichments
406 (Table 1, left-hand side). Compared to LBC, HBC logically dominate the total biomass by a 4-
407 fold ratio (+300%) in summer, and almost double by +80% in winter (Table 1, and Fig. S3a). The
408 importance of HBC is still high in the offshore domain in summer (+97%), while almost no
409 difference is observed (+7%) in winter during the productive season (see Fig. S3b for more
410 details). The annual cumulative biomass index associated with the HBC represents 88% of the
411 coastal domain, despite a corresponding coastline fraction of 42%. Because of the relative
412 importance of the winter period (December to March) in the productive season, we summarised
413 the overall significance of the coastal sector by its ratio to the offshore sector (Table 1, right-

hand side). This ratio shows that the coastal domain slightly dominates from January to February in both LBC and HBC (respective values of 0.64 and 0.73). Nevertheless, this ratio strongly increases in the adjacent months (December and March), with values of 2.57 and 4.14 for LBC and HBC respectively, highlighting the importance of HBC in coastal areas.

4.1.3 Large scale longitudinal variability

We specifically examined three profiles of the average biomass index and the MLD and TKE (Fig. 10), both averaged from the coast to 80 km offshore, to explore the longitudinal variability of the phytoplankton biomass over the year. Three cross-shore transects from the coastline to 80 km offshore were examined at three longitudes (1°W, 4.5°E and 7.5°E, blue dashed line in Fig. 8a). They were chosen because of their independence from the observed enrichments in the coastal domain (Fig. 8c).

Firstly, the results show a substantial eastward decrease in the intensity of the productive season, as shown by the biomass index (Fig. 10, orange bars), with annual cumulative values of 285, 152 and 86 g m^{-2} from West to East. This quantifies well the observations of a progressive decrease in the influence of the rich Atlantic waters eastward, following its progressive nutrient depletion. The shape of the productive season is stable at 1°W and 4.5°E, with a variable maximum centred at the first fortnight of February. A precise computation of this chronology along the entire Algerian coast (data not shown) shows that this central position is relatively stable from 1°W to 8.7°E (with minor variability <1 fortnight). In contrast, there is a positive shift of almost a fortnight (first fortnight of March) between 3°W and 1°W near the Alboran Sea, where a maximum shift of two fortnights is observed (data not shown). The productive season is more extended, due to the higher nutrient content of Atlantic waters.

We know that winter mixing due to wind and currents is the main cause of nutrient availability in the euphotic layer of the region (Conan et al., 2018; Fernandez et al., 2006; Kessouri et al., 2018; Millot, 1989). A close relationship was effectively observed between the seasonality of the MLD

and, to a lesser extent, the TKE (see Fig. S1 for spatial mapping of these two parameters) and the dynamics of the productive season captured by the biomass index. The MLD deepens eastwards with a simultaneous winter maximum (45 m to 60 m, see Fig. S1a) from January to February while the Modified Atlantic Waters (MAW) are drifted eastwards (Font et al., 1998). The productive season follows the winter mixing (average MLD >20 m, blue line) by about one month in the western and central part of the region (Fig. 10a-b). At the same time, a relative synchrony is progressively reached further East (Fig. 10c). The TKE (computed from geostrophic currents, i.e., including eddy energy and permanent currents) is almost permanently high at 1°W near the Alboran Sea (Fig. 10a) and not in phase with the biomass index.

It is very likely that, along with the significant enrichment effect of the MAW, water mixing is an important factor in the initiation of surface productivity but is probably not a limiting factor near the Alboran Sea with high-energy levels related to both Alboran gyres. Lower energy levels are observed further East at 4.5°E (Fig. 10b) with a slight relationship to the biomass index, while a higher association is observed at 7.5°E (Fig. 10c). This well-defined seasonal pattern explains that the higher MLD (50 to 60 m) observed in January-February, induces a rapid mixing of surface waters and a rapid increase in planktonic biomass during the second half of February. Average wind speed (data not shown) do not show any relationship with the surface water mixing, with low winter wind values from October to February. The MAW trajectory determines the large-scale variability of planktonic biomass in the AB. It is strongly constrained by nutrient availability, while the different sources of coastal enrichment represent a significant contribution throughout the year and unexpected relative importance of about two-thirds during the central part of the productive season and progressively higher during the rest of the year.

4.2 Sources of coastal enrichment

Previous studies using Chl-*a* variability as a proxy of the phytoplankton biomass variability along the Algerian basin have focused on large spatial scales, mainly over the continental shelf

464 (Mayot et al., 2016; Pieri et al., 2015; Salgado-Hernanz et al., 2019). They have generally
465 ignored small scales and coastal waters, except locally for sanitary purposes or risk assessment.
466 The annual average of the I_B averaged spatially from all seasons was calculated in the coastal
467 domain (0-10 km, green curve in Fig. 11) and in the offshore domain (beyond 10 km, blue curve
468 in Fig.11). The ratio (I_B Coastal/I_B Offshore) is considered a relative indicator of the local coastal
469 enrichment (red curve in Fig. 11). The I_B coastal peaks are variable in space and time (Fig. 11)
470 and indicate many distinct anomalies. In the Arzew, Bou-Ismaïl, Algiers and Annaba bays, the I_B
471 average is >20 g m^{-2} throughout the seasons (Fig. 11). These anomalies correspond mainly to
472 sandy coasts (orange bars in Fig. 11). It is important to note that many microphytobenthos
473 species (some diatoms, cyanobacteria, chlorophyceae and/or flagellates) prefer shallow sandy
474 coastal environments for their development (Cook and Røy, 2006; Hassan et al., 2006).
475 Nevertheless, the origin of these high production areas remains unclear.

476 Several bays are associated with wadis (temporary rivers) in many locations along the coast (in
477 blue in Fig. 11). These wadis are characterised by shallow flows (Fig. 12), generally <15 m^3 s^{-1}
478 during all year seasons. For example, in the Bou-Ismaïl Bay (Fig. 12a), the Mazafran flow varies
479 from <4 m^3 s^{-1} in summer (June to October) and from 4 to 13 m^3 s^{-1} in winter. In Algiers Bay
480 (Fig. 12b), the El-Harrach flow presents a very similar pattern. The Algiers city is affected by
481 intensive urbanisation (~70% of the coastline up to 800 m inland is urbanised), which has caused
482 significant environmental degradation of the coastal area and impacted the coastal morphology
483 (Rabehi et al., 2019). In Annaba Bay, the Seybouse wadi (Fig. 11, wadi 1) input is highly
484 concentrated in PO_4 and NH_4 compared to Mediterranean rivers (Ounissi et al., 2014), and
485 presents a potential risk of eutrophication (Ziouch et al., 2020). The observed peaks of Chl-*a*
486 (and I_B) are associated with different contributions (Table 2): the type of coast (sandy and rocky),
487 the presence of wadis and large cities, and the presence of bays.

488 In many cases, coastal enrichments are not the result of a single factor: for example, a biomass

489 peak is observed at 7.3°E associated with a wadi (wadi 2). The peak disappears shortly at 7.5°E,
490 despite the presence of sandy coast. In Oran Bay, a coastal peak is observed despite the absence
491 of a sandy coast and wadis (Fig. 11). However, Oran is a large city (>100,000 inhabitants) (Fig.
492 11), that induces a significant marine pollution due to wastewater discharged into the sea,
493 increasing nutrients in coastal waters. Another enrichment is observed at approximately 1.3°W,
494 where floating aquaculture cages are installed (Fig. 11). These aquaculture facilities are
495 considered a significant source of local enrichment (Cao et al., 2007). The low flows of the
496 wadis on the Algerian coast suggest that suspended matter (SM) from terrestrial inputs is weak in
497 coastal waters. In contrast, a significant source of SM may originate from local sediment
498 resuspension, especially on sandy coasts, where sediment resuspension generates a considerable
499 flux of nutrients (Robinson and Hill, 2005).

500 It is also known that the inner part of gulfs and bays trap nutrients from territorial inputs by
501 modifying local hydrodynamics that limit nutrient dispersal, thus maintaining high coastal
502 production with little influence on offshore production. It is important to note that, all previous
503 studies (Colella et al., 2016; Okubo, 1973; Pingree and Maddock, 1979; Signell and Geyer,
504 1991; Taillandier et al., 2020; Wolanski and Hamner, 1988) never considered potential coastal
505 influences. In winter and early spring, the richer coastal waters are often mixed with the offshore
506 waters and therefore contribute to the production beyond the continental shelf up to 10 km from
507 the coast, as shown by our biomass index.

508 **4.3 Modelling approach**

509 As previously mentioned, the Algerian coastal waters were divided into two classes: HBC (High-
510 Biomass Coastal Zones) and LBC (Low-Biomass Coastal Zones) (Fig. 11). The HBCs
511 consequently refer to the highest values of Chl-*a* and I_B, and the LBCs to the lowest values.
512 Their separation into two classes was visually optimised by defining specific thresholds for Chl-
513 *a* and I_B variables, summarised in Table 3 (response variables). We defined three qualitative

514 variables: the presence of wadis, the type of coast (sandy/rocky), and the existence of a Bay. The
515 City is defined as a quantitative variable with four levels: 0 (no-city), 25 k, 75 k, and 200 k
516 inhabitants.

517 Table 2 summarises the respective characteristics of LBC (numbered 1-16) and HBC (numbered
518 1-15) as manually selected in Fig. 11. The presence of Cities, Wadis and Bays are positively
519 related to the detection of High-biomass coastal areas. At the same time, the type of coast
520 appears to be irrelevant, mainly compared to the presence of a Bay.

521 Linear qualitative models (General Linear Models) were performed to evaluate the interactions
522 between either the coastal Chl-*a* concentration or the biomass index (I_B) and the four explanatory
523 variables, as shown in Table 3. The two specific areas HBC-1 and HBC-8 were excluded from
524 the modelling because these two areas are specifically influenced by aquaculture floating cages
525 that are not associated with the explanatory variables. A general model (m1 in Tab. 3) is first
526 tested by combining all seasons to test the separation between HBC and LBC, as presented in
527 Fig. 11. This model explains 67% of the variability, with a unique City effect. The Wadi effect is
528 absent, probably because of its association with City. On the opposite, in winter, the Chl-*a*
529 response variable (m2 model, 79%) is primarily associated with the presence of a Wadi, then to
530 City. In contrast, the I_B response variable (m3 model) is mainly related to a Bay and City
531 presence. The winter I_B model (m3) is very similar in explaining the biomass variability (77%),
532 with a dominance of City presence (as previously with Chl-*a*) as well as to a significant Bay
533 effect. In these winter models, the Wadi effect is only evidenced by the Chl-*a* variable that most
534 reflects the influence of local enrichments rather than their spatial extension, associated with the
535 biomass index (I_B), highlighting the Bay effect.

536 During summer (low-biomass season), the Chl-*a* based model (m4 in Tab. 3) shows only 57% of
537 explanation, with a unique Wadi effect despite the generally low flow of wadis in winter (Fig.
538 12). The equivalent model for the biomass index (m5) explains 78% of the variability, with a

dominance of Bay presence, while the Wadi effect is still present. The lower biomass variability in summer (not shown) is better explained by the spatially integrated biomass index (I_B). The later highlights a Bay effect, even if the main variability of the coastal enrichments is probably dominated by wadis and underneath by the influence of cities sewage.

Therefore, we can argue that anthropic effects (presence of a City and a Wadi) dominate the biomass variability in the coastal areas along the Algerian coast, much more than "natural" effects such as the coast type and the presence of a bay. However, the presence of Bay is also of primary importance for trapping enriched water within the coastal domain. Another significant point is undoubtedly the strong positive effect of aquaculture cages in two specific country locations (Fig. 11). It is noteworthy that marine aquaculture has developed considerably over the last decade, with a national initiative plan whose objective was to produce 100,000 tonnes of fish and shellfish by 2020 horizon (FAO, 2019).

5. Conclusion

Satellite-based Chl-*a* is an important proxy of phytoplanktonic biomass that allows us to disentangle very different dynamics between the coastal and offshore domains of the Algerian Basin (AB), characterised by a very narrow continental shelf. We show that a specific fortnightly climatology of 1-km resolution Chl-*a* generated from MODIS data makes possible this identification. The AB is characterised by two extreme high and low biomass seasons, separated by short 2-month transition periods. The offshore variability is closely related to large-scale processes governed by the influence of Atlantic waters and a progressive eastward decrease in biomass. The coastal domain reveals a very distinct dynamic associated with highly productive hotspots rather than a well-defined seasonality. The irregular morphology and nature of the Algerian coast (bays, gulfs, rocky or sandy coasts) is shaped by numerous terrestrial and temporary inputs that affect its local productivity. A Chl-*a* based spatially integrated index allows

us to quantify the importance of these coastal enrichments. At the same time, a modelling approach shows that seasonal wadis and city sewages, along with the presence of a bay, explain up to 79% of the presence of these productive hotspots. A separate source of enrichment is undoubtedly associated with the recent presence of aquaculture cages. Finally, considering phytoplanktonic communities and the in-situ determination of water quality would be beneficial to understand the biological consequences of these enrichments.

Acknowledgements

We applied the SDC (**S**equence **D**etermines **C**redit) approach for the sequence of authors. We would like to thank the space agency NASA for providing the MODIS satellite images used in this paper (https://oceancolor.gsfc.nasa.gov/). The authors are grateful to the whole team of the SOMBA-2014 cruise for providing the in-situ data used in this work. We thank the three anonymous reviewers for their helpful suggestions that greatly improved this manuscript. The combination of three funding sources supported this research: a PhD scholarship from the MESRS (Algerian government), a PhD scholarship from the Algerian-French program PROFAS B+ 2018-2019 (MERS-Algeria) and a partnership project (IRD-French) Fellowship.

References

Amores, A., Monserrat, S., Marcos, M., 2013. Vertical structure and temporal evolution of an anticyclonic eddy in the Balearic Sea (western Mediterranean): DESCRIPTION OF AN EDDY (BALEARIC SEA). J. Geophys. Res. Oceans 118, 2097–2106. https://doi.org/10.1002/jgrc.20150

Antoine, D., Morel, A., André, J.-M., 1995. Algal pigment distribution and primary production in the eastern Mediterranean as derived from coastal zone color scanner observations. J. Geophys. Res. 100, 16193. https://doi.org/10.1029/95JC00466

Barale, V., Garcia-Gorriz, E., Hoepffner, N., Stips, A., 2008. Near-Coastal Features of the NW Mediterranean Sea - Space and Time Heterogeneity of Atmospheric Forcing, Vertical Mixing and Algal Blooming, from Satellite Observations and Model Simulations (1997-2007). https://doi.org/10.13140/RG.2.1.2425.9285

Béranger, K., Mortier, L., Crépon, M., 2005. Seasonal variability of water transport through the Straits of Gibraltar, Sicily and Corsica, derived from a high-resolution model of the Mediterranean circulation. Progress in Oceanography, Mediterranean physical oceanography and biogeochemical cycles: Mediterranean general circulation and climate variability 66, 341–364. https://doi.org/10.1016/j.pocean.2004.07.013

Bethoux, J.P., Durieu de Madron, X., Nyffeler, F., Tailliez, D., 2002. Deep water in the western Mediterranean: peculiar 1999 and 2000 characteristics, shelf formation hypothesis, variability since 1970 and geochemical inferences. Journal of Marine Systems 33–34, 117–131. https://doi.org/10.1016/S0924-7963(02)00055-6

Cao, L., Wang, W., Yang, Y., Yang, C., Yuan, Z., Xiong, S., Diana, J., 2007. Environmental Impact of Aquaculture and Countermeasures to Aquaculture Pollution in China. Env Sci Pollut Res 11. http://dx.doi.org/10.1065/espr2007.05.426

Cerino, F., Fornasaro, D., Kralj, M., Giani, M., Cabrini, M., 2019. Phytoplankton temporal dynamics in the coastal waters of the north-eastern Adriatic Sea (Mediterranean Sea) from 2010 to 2017. NC 34, 343–372. https://doi.org/10.3897/natureconservation.34.30720

Colella, S., Falcini, F., Rinaldi, E., Sammartino, M., Santoleri, R., 2016. Mediterranean Ocean Colour Chlorophyll Trends. PLoS One 11. https://doi.org/10.1371/journal.pone.0155756

Conan, P., Testor, P., Estournel, C., D'Ortenzio, F., Durrieu de Madron, X., 2018. Observing Winter Mixing and Spring Bloom in the Mediterranean. Eos 99. https://doi.org/10.1029/2018EO105887

Cook, P.L.M., Røy, H., 2006. Advective relief of CO_2 limitation in microphytobenthos in highly productive sandy sediments. Limnology and Oceanography 51, 1594–1601. https://doi.org/10.4319/lo.2006.51.4.1594

Crispi, G., Pacciaroni, M., 2009. Long-term numerical evolution of the nitrogen bulk content in the Mediterranean Sea. Estuarine, Coastal and Shelf Science 83, 148–158. https://doi.org/10.1016/j.ecss.2007.12.015

Cullen, J.J., 1982. The Deep Chlorophyll Maximum: Comparing Vertical Profiles of Chlorophyll *a*. Can. J. Fish. Aquat. Sci. 39, 791–803. https://doi.org/10.1139/f82-108

Demarcq, H., Barlow, R., Hutchings, L., 2007. Application of a chlorophyll index derived from satellite data to investigate the variability of phytoplankton in the Benguela ecosystem. African Journal of Marine Science 29, 271–282. https://doi.org/10.2989/AJMS.2007.29.2.11.194

D'Ortenzio, F., Ribera d'Alcalà, M., 2009. On the trophic regimes of the Mediterranean Sea: a satellite analysis. Biogeosciences 139–148. https://doi.org/10.5194/bg-6-139-2009

Elbaz-Poulichet, F., Guieu, C., Morley, N.H., 2001. A Reassessment of Trace Metal Budgets in the Western Mediterranean Sea. Marine Pollution Bulletin 42, 623–627. https://doi.org/10.1016/S0025-326X(01)00065-0

El-Geziry, T.M., Bryden, I.G., 2010. The circulation pattern in the Mediterranean Sea: issues for modeller consideration. Journal of Operational Oceanography 3, 39–46. https://doi.org/10.1080/1755876X.2010.11020116

Fani, F., Nuccio, C., Lazzara, L., Massi, L., Battocchi, C., Penna, A., 2014. Fibrocapsa japonica (Raphidophyceae) occurrence and ecological features within the phytoplankton assemblage of a cyclonic eddy, offshore the Eastern Alboran Sea. Medit. Mar. Sci. 15, 250. https://doi.org/10.12681/mms.398

FAO, 2019. FAO Fisheries & Aquaculture - Vue générale du secteur aquacole national - Algérie. National Aquaculture Sector Overview Fact Sheets. Texte par Oussaid, M. Dans: Division des pêches de la FAO [en ligne]. http://www.fao.org/fishery/countrysector/naso_algeria/fr#tcN700B1 (accessed 8.24.21).

Fernandez, V., Umlauf, L., Dobricic, S., Burchard, H., Nadia, P., 2006. Validation and intercomparison of two vertical-mixing schemes in the Mediterranean Sea. Ocean Science Discussions 3. https://doi.org/10.5194/osd-3-1945-2006

Fondriest Environmental, 2014. Sediment Transport and Deposition. Environmental Measurement Systems. https://www.fondriest.com/environmental-measurements/parameters/hydrology/sediment-transport-deposition/ (accessed 2.27.21).

Font, J., Millot, C., Salas, J., Julià, A., Chic, O., 1998. The drift of Modified Atlantic Water from the Alboran Sea to the eastern Mediterranean. SCIENTIA MARINA 62, 6. https://doi.org/10.3989/scimar.1998.62n3211

Google Maps, 2021. Algeria - Google Maps. https://www.google.com/maps/place/Alger (accessed 1.14.21).

Groom, S., Sathyendranath, S., Ban, Y., Bernard, S., Brewin, R., Brotas, V., Brockmann, C., Chauhan, P., Choi, J., Chuprin, A., Ciavatta, S., Cipollini, P., Donlon, C., Franz, B., He, X., Hirata, T., Jackson, T., Kampel, M., Krasemann, H., Lavender, S., Pardo-Martinez, S., Mélin, F., Platt, T., Santoleri, R., Skakala, J., Schaeffer, B., Smith, M., Steinmetz, F., Valente, A., Wang, M., 2019. Satellite Ocean Colour: Current Status and Future Perspective. Front. Mar. Sci. 6, 485. https://doi.org/10.3389/fmars.2019.00485

Harid, R., Ait Kaci, M., Keraghel, M.A., Zerroukı, M., Houma-Bachari, F., 2018. Seasonal and Interannual Variability of Primary Production and Chlorophyll Concentrations in the Algerian Basin: Application of Ocean Color, in: Kallel, A., Ksibi, M., Ben Dhia, H., Khélifi, N. (Eds.), Recent Advances in Environmental Science from the Euro-Mediterranean and Surrounding Regions, Advances in Science, Technology & Innovation. Springer International Publishing, Cham, pp. 1641–1643. https://doi.org/10.1007/978-3-319-70548-4_475

Hassan, G.S., Espinosa, M.A., Isla, F.I., 2006. Modern Diatom Assemblages in Surface Sediments from Estuarine Systemsin the Southeastern Buenos Aires Province, Argentina. J Paleolimnol 35, 39. https://doi.org/10.1007/s10933-005-6444-8

Houpert, L., Testor, P., Durrieu de Madron, X., Somot, S., D'Ortenzio, F., Estournel, C., Lavigne, H., 2015. Seasonal cycle of the mixed layer, the seasonal thermocline and the upper-ocean heat storage rate in the Mediterranean Sea derived from observations. Progress in Oceanography 132, 333–352. https://doi.org/10.1016/j.pocean.2014.11.004

Huertas, I.E., Ríos, A.F., García-Lafuente, J., Navarro, G., Makaoui, A., Sánchez-Román, A., Rodriguez-Galvez, S., Orbi, A., Ruíz, J., Pérez, F.F., 2012. Atlantic forcing of the Mediterranean oligotrophy: ATLANTIC FORCING OF MEDITERRANEAN OLIGOTROPHY. Global Biogeochem. Cycles 26, n/a-n/a. https://doi.org/10.1029/2011GB004167

Huertas, I.E., Rıos, A.F., Garcıa-Lafuente, J., Makaoui, A., Rodrıguez-Galvez, S., Sanchez-Roman, A., Orbi, A., Ruız, J., Perez, F.F., 2009. Anthropogenic and natural CO2 exchange through the Strait of Gibraltar. Biogeosciences 6, 647–662. https://doi.org/10.5194/bg-6-647-2009

Keraghel, M.A., Louanchi, F., Zerrouki, M., Aït Kaci, M., Aït-Ameur, N., Labaste, M., Legoff, H., Taillandier, V., Harid, R., Mortier, L., 2020. Carbonate system properties and anthropogenic carbon inventory in the Algerian Basin during SOMBA cruise (2014): Acidification estimate. Marine Chemistry 221, 103783. https://doi.org/10.1016/j.marchem.2020.103783

Kessouri, F., Ulses, C., Estournel, C., Marsaleix, P., D'Ortenzio, F., Severin, T., Taillandier, V., Conan, P., 2018. Vertical Mixing Effects on Phytoplankton Dynamics and Organic Carbon Export in the Western Mediterranean Sea. J. Geophys. Res. Oceans 123, 1647–1669. https://doi.org/10.1002/2016JC012669

Khatiwala, S., Tanhua, T., Mikaloff Fletcher, S., Gerber, M., Doney, S.C., Graven, H.D., Gruber, N., McKinley, G.A., Murata, A., Ríos, A.F., Sabine, C.L., 2013. Global ocean storage of anthropogenic carbon. Biogeosciences 10, 2169–2191. https://doi.org/10.5194/bg-10-2169-2013

Lavigne, H., D'Ortenzio, F., Ribera D'Alcalà, M., Claustre, H., Sauzède, R., Gacic, M., 2015. On the vertical distribution of the chlorophyll <i>a</i> concentration in the Mediterranean Sea: a basin scale and seasonal approach. Biogeosciences Discuss. 12, 4139–4181. https://doi.org/10.5194/bgd-12-4139-2015

Lazzari, P., Solidoro, C., Ibello, V., Salon, S., Teruzzi, A., Béranger, K., Colella, S., Crise, A., 2012. Seasonal and inter-annual variability of plankton chlorophyll and primary production in the Mediterranean Sea: a modelling approach. Biogeosciences 9, 217–233. https://doi.org/10.5194/bg-9-217-2012

Marañón, E., Van Wambeke, F., Uitz, J., Boss, E.S., Pérez-Lorenzo, M., Dinasquet, J., Haëntjens, N., Dimier, C., Taillandier, V., 2020. Deep maxima of phytoplankton biomass, primary production and bacterialproduction in the Mediterranean Sea during late spring (preprint). Biodiversity and Ecosystem Function: Microbial Ecology & Geomicrobiology. https://doi.org/10.5194/bg-2020-261

Mayot, N., D'Ortenzio, F., Ribera d'Alcalà, M., Lavigne, H., Claustre, H., 2016. Interannual variability of the Mediterranean trophic regimes from ocean color satellites. Biogeosciences 13, 1901–1917. https://doi.org/10.5194/bg-13-1901-2016

Millot, C., 1999. Circulation in the Western Mediterranean Sea. Journal of Marine Systems 20, 423–442. https://doi.org/10.1016/S0924-7963(98)00078-5

Millot, C., 1989. La circulation générale en Méditerranée occidentale : Aperçu de nos connaissances et projets d'études. geo 98, 497–515. https://doi.org/10.3406/geo.1989.20925

Millot, C., Taupier-Letage, I., 2005. Circulation in the Mediterranean Sea. Hdb Env Chem 5, 38. https://doi.org/DOI 10.1007/b107143

Millot, C., Taupier-Letage, I., Benzohra, M., 1990. The Algerian eddies. Earth-Science Reviews 27, 203–219. https://doi.org/10.1016/0012-8252(90)90003-E

Morel, A., Prieur, L., 1977. Analysis of variations in ocean color1: Ocean color analysis. Limnol. Oceanogr. 22, 709–722. https://doi.org/10.4319/lo.1977.22.4.0709

Mortier, L., AIt Ameur, N., Taillandier, V., 2014. SOMBA-GE-2014 cruise,Téthys II R/V. https://doi.org/10.17600/14007500

Moutin, T., Prieur, L., 2012. Influence of anticyclonic eddies on the Biogeochemistry from the Oligotrophic to the Ultraoligotrophic Mediterranean (BOUM cruise). Biogeosciences 9, 3827–3855. https://doi.org/10.5194/bg-9-3827-2012

NASA's Ocean Color Web, 2019. Available online: http://oceancolor.gsfc.nasa.gov/ (accessed on 29 October 2019).

Okubo, A., 1973. Effect of shoreline irregularities on streamwise dispersion in estuaries and other embayments. Netherlands Journal of Sea Research 6, 213–224. https://doi.org/10.1016/0077-7579(73)90014-8

Olita, A., Sorgente, R., Ribotti, A., Fazioli, L., Perilli, A., 2011. Pelagic primary production in the Algero-Provençal Basin by means of multisensor satellite data: focus on interannual variability and its drivers. Ocean Dynamics 61, 1005–1016. https://doi.org/10.1007/s10236-011-0405-8

O'Reilly, J.E., Werdell, P.J., 2019. Chlorophyll algorithms for ocean color sensors - OC4, OC5 & OC6. Remote Sensing of Environment 229, 32–47. https://doi.org/10.1016/j.rse.2019.04.021

Ounissi, M., Ziouch, O.-R., Aounallah, O., 2014. Variability of the dissolved nutrient (N, P, Si) concentrations in the Bay of Annaba in relation to the inputs of the Seybouse and Mafragh estuaries. Marine Pollution Bulletin 80, 234–244. https://doi.org/10.1016/j.marpolbul.2013.12.030

Palmiéri, J., Dutay, J.-C., D'Ortenzio, F., Houpert, L., Mayot, N., Bopp, L., 2018. The Mediterranean subsurface phytoplankton dynamics and their impact on Mediterranean bioregions. Biogeosciences Discussions 1–38. https://doi.org/10.5194/bg-2018-423

Pasqueron de Fommervault, O., D'Ortenzio, F., Mangin, A., Serra, R., Migon, C., Claustre, H., Lavigne, H., Ribera d'Alcalà, M., Prieur, L., Taillandier, V., Schmechtig, C., Poteau, A., Leymarie, E., Dufour, A., Besson, F., Obolensky, G., 2015. Seasonal variability of nutrient concentrations in the M editerranean S ea: Contribution of B io- A rgo floats. J. Geophys. Res. Oceans 120, 8528–8550. https://doi.org/10.1002/2015JC011103

Peliz, Á., Teles-Machado, A., Marchesiello, P., Dubert, J., Lafuente, J.G., 2009. Filament generation off the Strait of Gibraltar in response to Gap winds. Dynamics of Atmospheres and Oceans 46, 36–45. https://doi.org/10.1016/j.dynatmoce.2008.08.002

Pessini, F., Cotroneo, Y., Olita, A., Sorgente, R., Ribotti, A., Jendersie, S., Perilli, A., 2020. Life history of an anticyclonic eddy in the Algerian basin from altimetry data, tracking algorithm and in situ observations. Journal of Marine Systems 207, 103346. https://doi.org/10.1016/j.jmarsys.2020.103346

Pessini, F., Olita, A., Cotroneo, Y., Perilli, A., 2018. Mesoscale eddies in the Algerian Basin: do they differ as a function of their formation site? Ocean Sci. 14, 669–688. https://doi.org/10.5194/os-14-669-2018

Pieri, M., Massi, L., Lazzara, L., Nuccio, C., Lapucci, C., Maselli, F., 2015. Assessment of three algorithms for the operational estimation of [CHL] from MODIS data in the Western Mediterranean Sea. European Journal of Remote Sensing 48, 383–401. https://doi.org/10.5721/EuJRS20154822

Pingree, R.D., Maddock, L., 1979. The tidal physics of headland flows and offshore tidal bank formation. Marine Geology 32, 269–289. https://doi.org/10.1016/0025-3227(79)90068-9

Rabehi, W., Guerfi, M., Mahi, H., 2019. La baie d'Alger, un espace côtier prisé, entre pressions d'urbanisation et gouvernance territoriale. Geo-Eco-Marina 25, 113–130. https://doi.org/10.5281/ZENODO.3609744

Robinson, A.R., Hill, M.N. (Eds.), 2005. Biological-physical interactions in the sea, 1. Harvard Univ. Press publication 2005. ed, The sea The global coastal ocean. Harvard Univ. Press, Cambridge, Mass.

Salgado-Hernanz, P.M., Racault, M.-F., Font-Muñoz, J.S., Basterretxea, G., 2019. Trends in phytoplankton phenology in the Mediterranean Sea based on ocean-colour remote sensing. Remote Sensing of Environment 221, 50–64. https://doi.org/10.1016/j.rse.2018.10.036

Signell, R.P., Geyer, W.R., 1991. Transient eddy formation around headlands. Journal of Geophysical Research: Oceans 96, 2561–2575. https://doi.org/10.1029/90JC02029

Sobel, I., 1990. An Isotropic 3x3 Gradient Operator, Machine Vision for Three Dimensional Scenes, Freeman, H. Academic Pres 376–379.

Strickland, J., 1965. Production of organic matter in primary stages of themarine food chain, in: Chemical Oceanography, Academic Press, London, edited by: J. P. Riley and G. Skirrow. Chemical Oceanography, Academic Press 477–610.

Taillandier, V., Prieur, L., D'Ortenzio, F., Ribera d'Alcalà, M., Pulido-Villena, E., 2020. Profiling float observation of thermohaline staircases in the western Mediterranean Sea and impact on nutrient fluxes (preprint). Biogeochemistry: Open Ocean. https://doi.org/10.5194/bg-2019-504

Taupier-Letage, I., 2003. Biological response to mesoscale eddies in the Algerian Basin. J. Geophys. Res. 108, 3245. https://doi.org/10.1029/1999JC000117

Taupier-Letage, Millot, C., 1988. Surface circulation in the Algerian basin during 1984. Oceanologia Acta 9, 79–85. https://archimer.ifremer.fr/doc/00267/37811/

Testor, P., Send, U., Gascard, J.-C., Millot, C., Taupier-Letage, I., Béranger, K., 2005. The mean circulation of the southwestern Mediterranean Sea: Algerian Gyres. Journal of Geophysical Research: Oceans 110. https://doi.org/10.1029/2004JC002861

Vargas-Yáñez, M., Zunino, P., Benali, A., Delpy, M., Pastre, F., Moya, F., García-Martínez, M. del C., Tel, E., 2010. How much is the western Mediterranean really warming and salting? Journal of Geophysical Research: Oceans 115. https://doi.org/10.1029/2009JC005816

Volpe, G., 2012. Seasonal to interannual phytoplankton response to physical processes in the Mediterranean Sea from satellite observations. Remote Sensing of Environment 13. https://doi.org/10.1016/j.rse.2011.09.020

Volpe, G., Colella, S., Brando, V., Forneris, V., La Padula, F., Di Cicco, A., Sammartino, M., Bracaglia, M., Artuso, F., Santoleri, R., 2018. The Mediterranean Ocean Colour Level 3 Operational Multi-Sensor Processing (preprint). Remote Sensing/Biological Processes/Surface/Mediterranean Sea. https://doi.org/10.5194/os-2018-73

Wolanski, E., Hamner, W.M., 1988. Topographically Controlled Fronts in the Ocean and Their Biological Influence. Science 241, 177–181. https://doi.org/10.1126/science.241.4862.177

Ziouch, O.R., Laskri, H., Chenaker, H., Ledjedel, N.E., Daifallah, T., Ounissi, M., 2020. Transport of nutrients from the Seybouse River to Annaba Bay (Algeria, SW Mediterranean). Marine Pollution Bulletin 156, 111231. https://doi.org/10.1016/j.marpolbul.2020.111231

Figure captions

Figure 1. March climatological average of the Chl-*a* concentration (mg m^{-3}) between 2003 and 2018 in the Algerian Basin (Mediterranean Sea). The average current velocity (m s^{-1}) for the same period (black arrows), the 800 m isobath (red line), and the 0.5 mg m^{-3} isopleth (dark green line) is superimposed. The stations of the SOMBA-2014 cruise are also superimposed (white dots). The large eddies in black (Alg. WG and Alg. EG) are deduced from the average sea level anomaly between 2003 and 2018. The average position of the Alboran eddies (Alb. WG and Alb. EG) are added.

Figure 2. Comparison of Chl-*a* concentration for the first fortnight of January (2003-2018 climatology) from (a) MODIS Level-3 data at 4-km resolution and (b) MODIS Level-2 (uncorrected data) at 1-km resolution.

Figure 3. Definition of the outlier pixels criteria for improving the cloud masking (example of 07 January 2014). (a) Local (3x3 matrix) Sobel gradient (mg m^{-3} km^{-1}). (b) Distance (D1) from the cloud borders, in km (clouds are in white). (c) Distance (D2) from the shoreline, in km. (d to f): Pixels identified as cloudy from,: (d) the gradient criteria, (e) the temporal variation (TV) criteria, (f) from isolated pixels within cloud (IP) criteria. The result of the combination of all three criteria is shown in (h) versus the original MODIS Level-2 data (g).

Figure 4. Linear relationship (red line) (a) between MODIS satellite corrected data (Y axis) and in-situ Chl-*a* data (X axis) during the SOMBA cruise (14 August to 10 September 2014) in the Algerian Basin. (b), (c), (d), and (e): spatial variability of the daily Chl-*a* field associated with four selected stations. The stations represented with a grey cross in (c) and (d) were removed from the comparison on the basis of a gradient threshold criteria or because their proximity to clouds.

Figure 5. Results of the elimination of outlier pixels from the original uncorrected MODIS Level-2 data (left column), respectively for a fortnightly average (example of 1-15/01/2014) (a and b), and for a monthly climatological average (example of January 2003-2018) (c and d).

Figure. 6. Hovmöller diagrams of the cross-shore seasonality (from the coast line to 120 km offshore) of the Chl-*a* concentration in the Algerian Basin averaged between 2.2°W and 8.7°E, from fortnightly climatologies (2003-2018) computed from (a) MODIS Level-3 data at 4-km resolution, (b) MODIS Level-2 corrected data at 1-km resolution. The black line separates the 10 km distance from the coast. (c) and (d) highlight the data for this coastal area. The average cross-shore profiles in March (green line) and August (blue line) are shown in (e) and (f).

Figure 7. Average seasonality of the Chl-*a* concentration from 2003 to 2018 in the Algerian Basin from fortnightly Chl-*a* averages (a) in the 0-10 km coastal sector (green plain line) and offshore (blue plain line). The corresponding 4-km resolution Chl-*a* MODIS data (dotted lines) as well as the depth of the mixed Layer (MLD, orange dasher line) are superimposed. (b) Zonally averaged cross-shore Chl-*a* transect from the coast to 50 km for the High-Biomass (green), the transition (yellow), and the Low-Biomass (blue) seasons. The horizontal line shows the 0.5 mg m^{-3} limit used to compute the integrated index, detailed in Fig. 8 and Fig. 9.

Figure 8. Time-space diagrams of the longitudinal variability (2.2°W to 8.7°E) of three Chl-*a* associated indices in the Algerian Basin from August to July. The four distances considered (a) were: the distance of 10 km from the coast (green line), the average maximum distance of the 0.5 mg m^{-3} isopleth, the$Dist_{0.5mg}^{max}$ (red line), the 80 km maximum distance allowed for I_B (gray solid line), and the middle distance from the northern coastlines (gray dashed line). (b) the distance from the coast of the Chl-*a* concentration ≥0.5 mg m^{-3}. (c) the Chl-*a* averaged over the same area. (d) the integrated biomass index (IB) from whole basin.

Figure 9. Time-space diagrams of the alongshore variability (2.2°W 8.7°E) of the Chl-*a* and biomass index I_B: (a) the Chl-*a* averaged in the coastal area (0-10 km) and (b) in the offshore area (10-$Dist_{0.5mg}^{max}$km), the biomass index (I_B) integrated from (c) the coastline to a maximum distance of 10 km, and (d) from 10 km to the maximum distance$Dist_{0.5mg}^{max}$.

Figure 10. Average seasonality of the integrated biomass index (orange bars) at three locations : 1°W (a), 4.5°E (b), and 7.5° (c) situated outside coastal influences (see Fig. 8a for precise locations). The climatological values of the Mixed Layer Depth (MLD, blue line), and the Total Kinetic Energy (TKE, black line) at the same locations are superimposed.

Figure 11. Longitudinal variability of the offshore (blue line) and coastal (green line) yearly averages of the integrated biomass index, with the "I_B coastal / offshore" ratio superimposed (red

line). Areas with high coastal biomass index are highlighted with green rectangles (1-15) by comparison with Low-Biomass coastal Chl-*a* areas (1-16) left blank. The wadis discharges, the coast type (sandy coast in yellow and rocky coast in blue), and the size of nearby cities (red dots) are superimposed. The coast type is deduced from the "Google Map" images (Google Maps, 2021). The wadis names are respectively : (1) Seybouse Wadi, (2) El-Kebir Wadi, (3) Z'Hor Wadi, (4) El-Kebir Wadi, (5) Soummam Wadi, (6) Bou-Douaou Wadi, (7) El-Hamiz Wadi, (8) El-Harrach Wadi, (9) Mazafran Wadi, (10) Cheliff Wadi, (11) El-Hammam Wadi.

Figure 12. Seasonal variability of the Mazafran and the El-harrach wadis flows (in $m^3\ s^{-1}$, orange line) and the corresponding Chl-*a* concentration (green line) averaged at the isobath <50 m from 2003 to 2012 : (a) in the Bou-Ismaïl bay and (b) in the Algiers bay. The maps (a' and b') show the Chl-*a* yearly average at each location.

Table 1. Spatially integrated biomass index (I_B, in $g\ m^{-2}$) seasonally cumulated between 2003 and 2018 for regions of high and low biomass (as displayed in Fig. 11) for the coastal and offshore domains. The last line shows the relative importance of the High vs Low I_B index and the right part of the table shows the ratio between the coastal and offshore domains for both types of regions.

Table 2. Summary of the characteristics of the LBC (numbered 1-16) and HBC (numbered 1-15) regions as manually selected in Fig. 11. Both Chl-*a* and I_B variables were averaged for each LBC (white rectangles, 1-16) and HBC (green rectangles, 1-15) of Fig. 11. The City size [0-3] is defined by respectively: 0 (no city), 1: [0 50k] inhabitants (small red dot), 2 [50k- 100k] (intermediate red dot), 3: >100k (large red dot). The Coast-type is either Sandy(S) or Rocky(R). The small black dots represent aquaculture cages.

Table 3. Parameters of the linear models calculated to evaluate the interactions between the coastal Chl-*a* biomass or the I_B index and the four aforementioned variables of different of

658 coastal enrichment sources. The averages of I_B and Chl-*a* in winter and summer are calculated

659 according to the High and the Low-Biomass months shown in Fig. 7a.

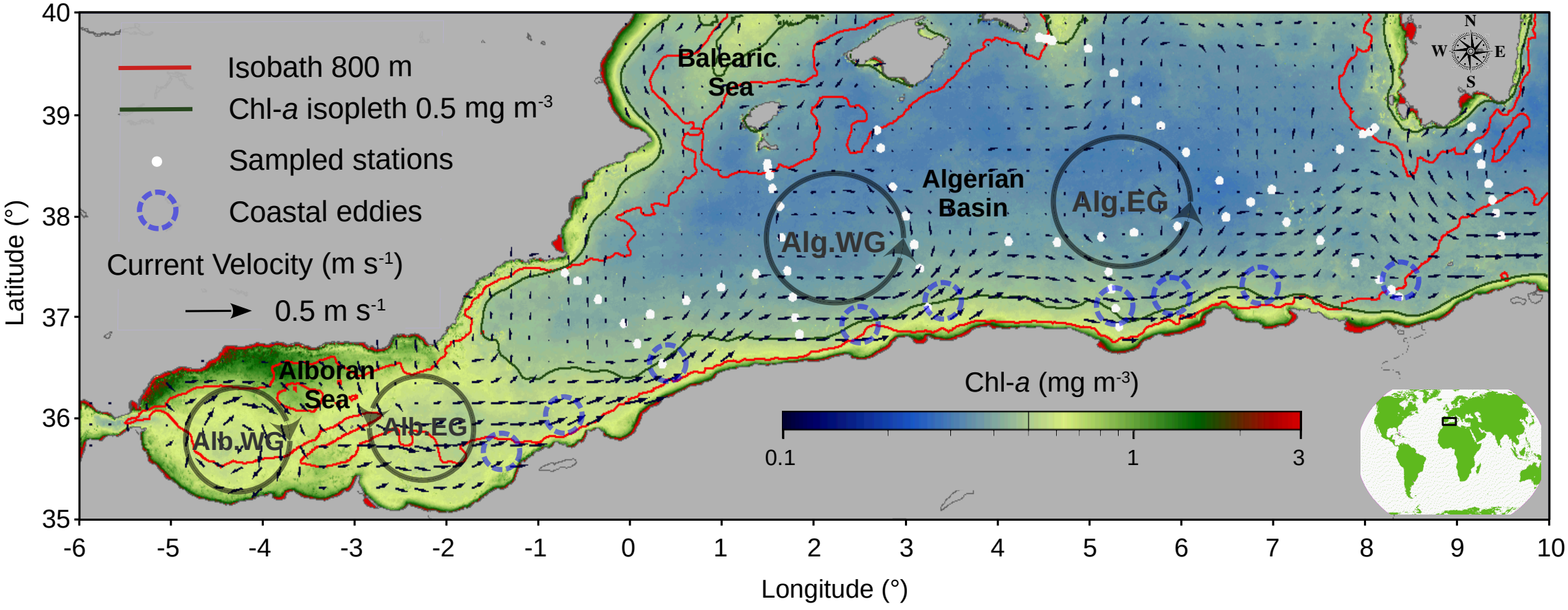
Isobath 800 m
Chl-a isopleth 0.5 mg m-3
Sampled stations
Coastal eddies
Current Velocity (m s-1)
0.5 m s-1
Balearic Sea
Algerian Basin
Alg.WG
Alg.EG
Alboran Sea
Alb.WG
Alb.EG
Chl-a (mg m-3)
0.1
1
3
N
W
E
S
Latitude (°)
Longitude (°)
40
39
38
37
36
35
-6
-5
-4
-3
-2
-1
0
1
2
3
4
5
6
7
8
9
10

a)

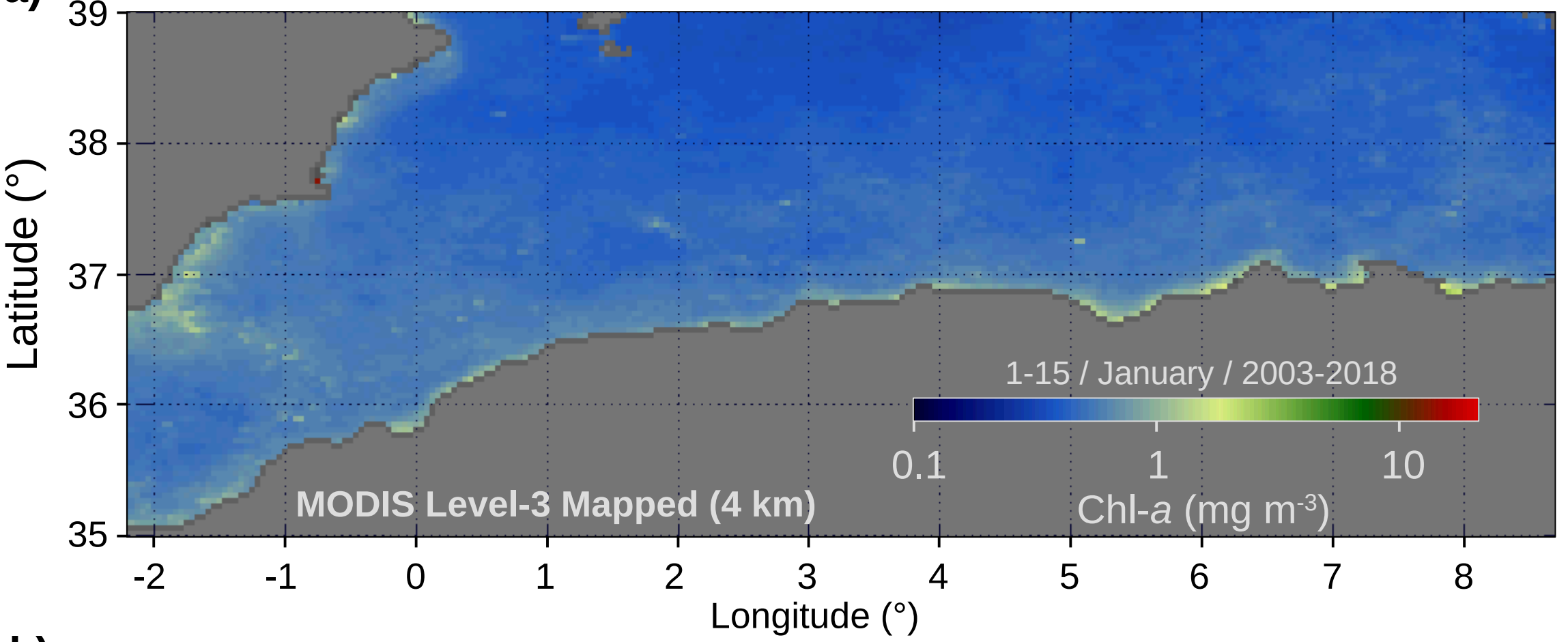
Latitude (°)
39
38
37
36
35
-2
-1
0
1
2
3
4
5
6
7
8
Longitude (°)
1-15 / January / 2003-2018
0.1
1
10
Chl-a (mg m-3)
MODIS Level-3 Mapped (4 km)

b)

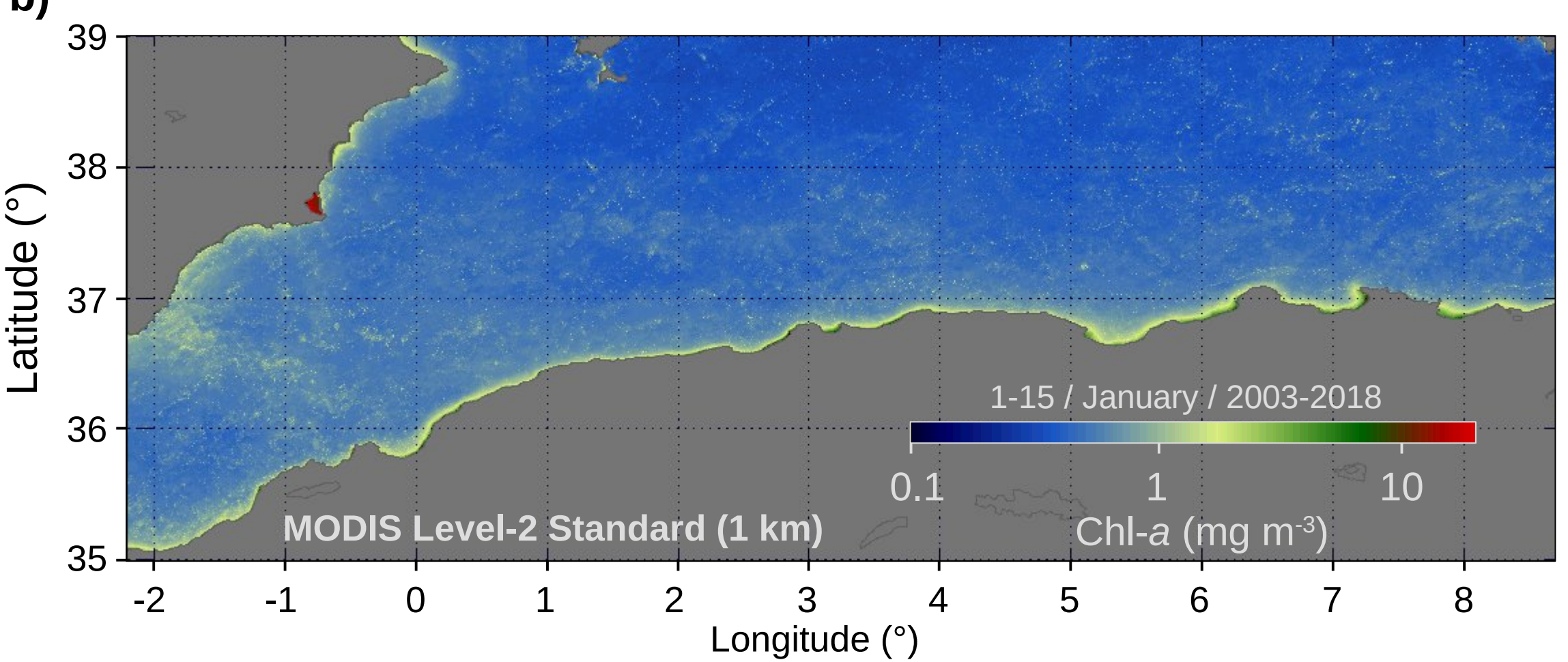
Latitude (°)
39
38
37
36
35
-2
-1
0
1
2
3
4
5
6
7
8
Longitude (°)
1-15 / January / 2003-2018
0.1
1
10
Chl-a (mg m-3)
MODIS Level-2 Standard (1 km)

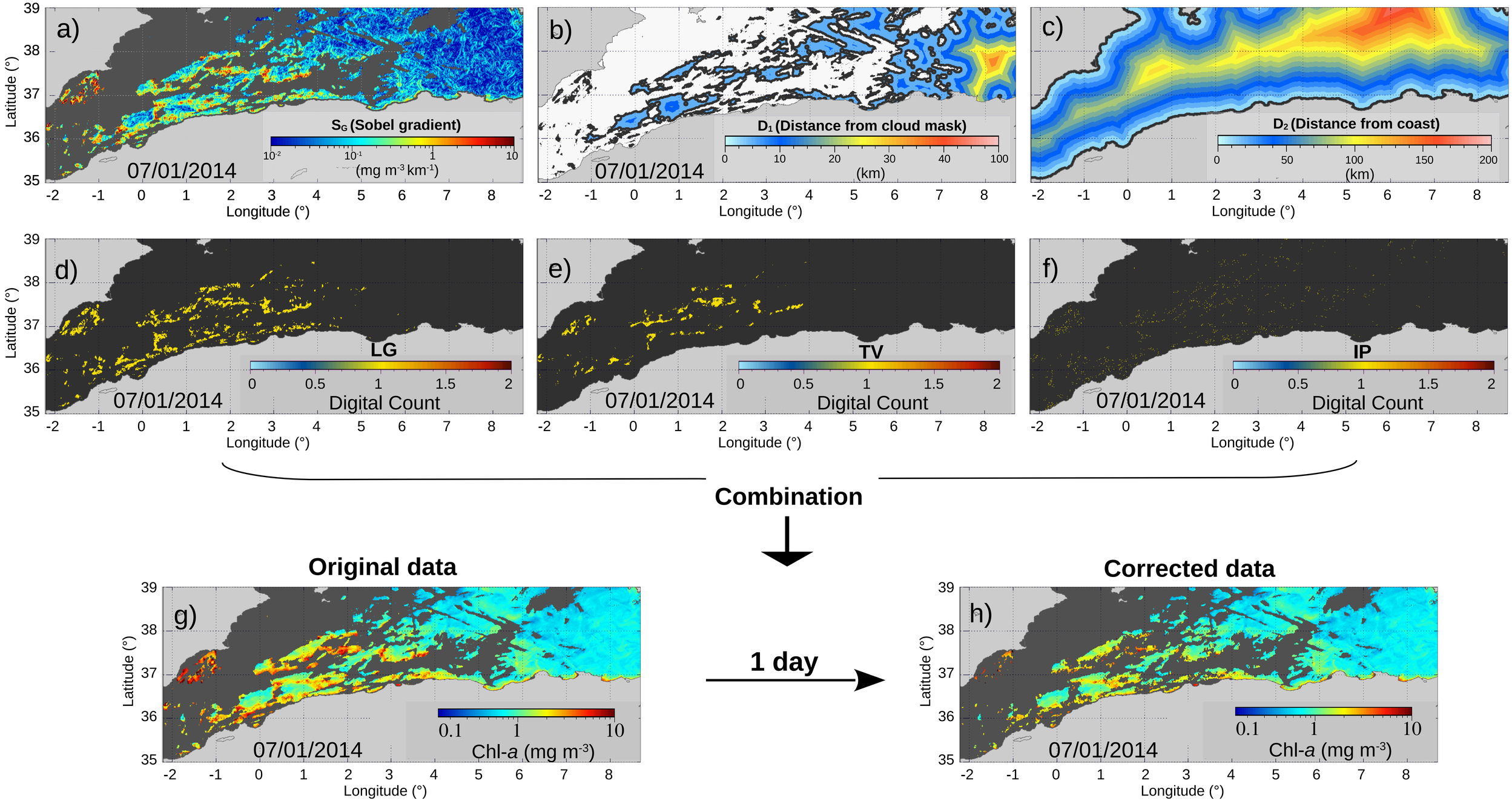
a)
S_G (Sobel gradient)
10^{-2} 10^{-1} 1 10
(mg m^{-3} km^{-1})
07/01/2014
b)
D_1 (Distance from cloud mask)
0 10 20 30 40 100
(km)
07/01/2014
c)
D_2 (Distance from coast)
0 50 100 150 200
(km)
d)
LG
0 0.5 1 1.5 2
Digital Count
07/01/2014
e)
TV
0 0.5 1 1.5 2
Digital Count
07/01/2014
f)
IP
0 0.5 1 1.5 2
Digital Count
07/01/2014
Latitude (°)
Longitude (°)
Combination
Original data
Corrected data
1 day
g)
h)
0.1 1 10
Chl-a (mg m^{-3})
07/01/2014

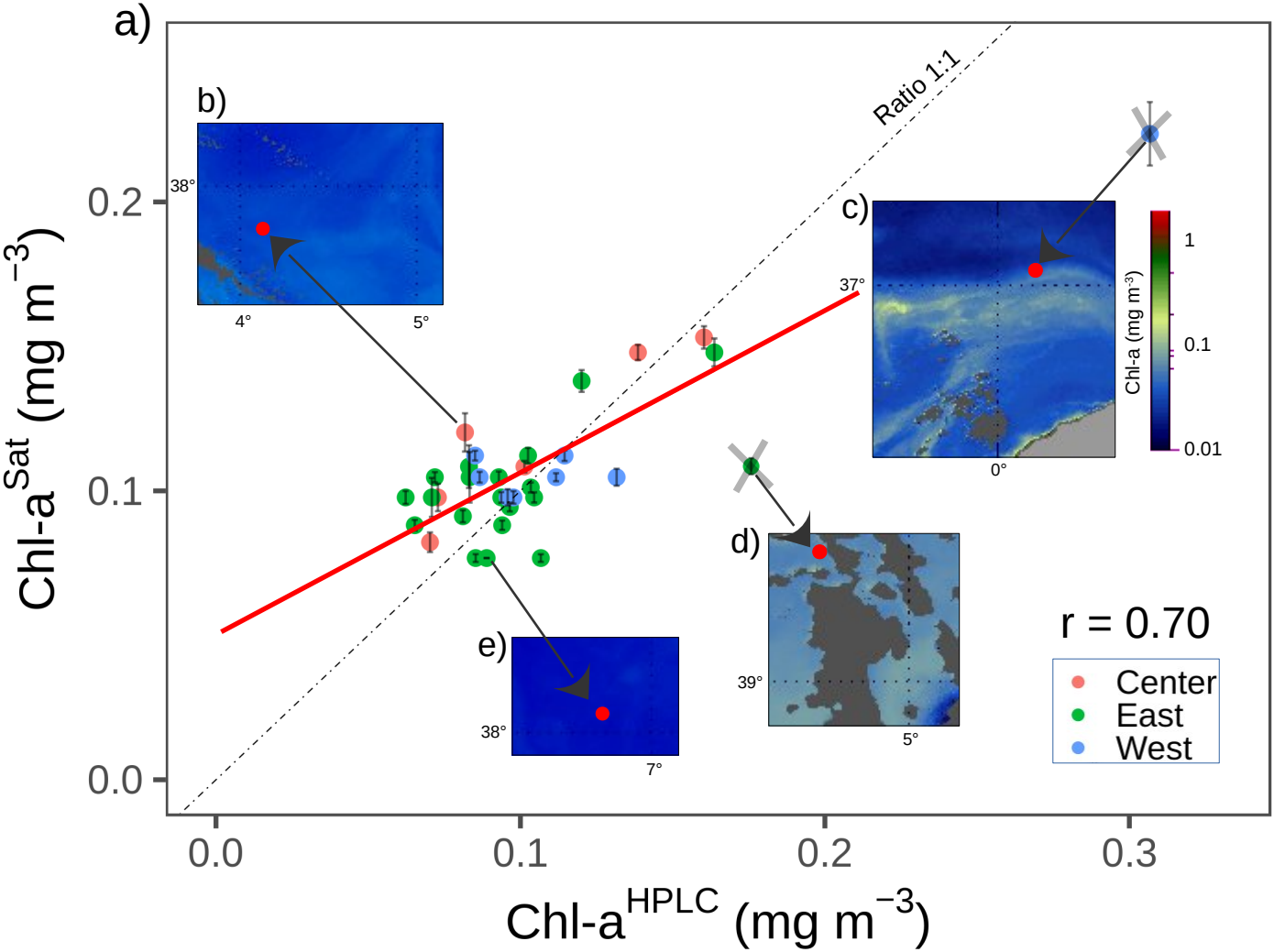
a)
b)
c)
d)
e)
Ratio 1:1
r = 0.70
Center
East
West
Chl-a (mg m-3)
1
0.1
0.01
38°
4°
5°
37°
0°
39°
38°
7°
0.0
0.1
0.2
0.3
Chl-a^Sat (mg m^-3)
Chl-a^HPLC (mg m^-3)

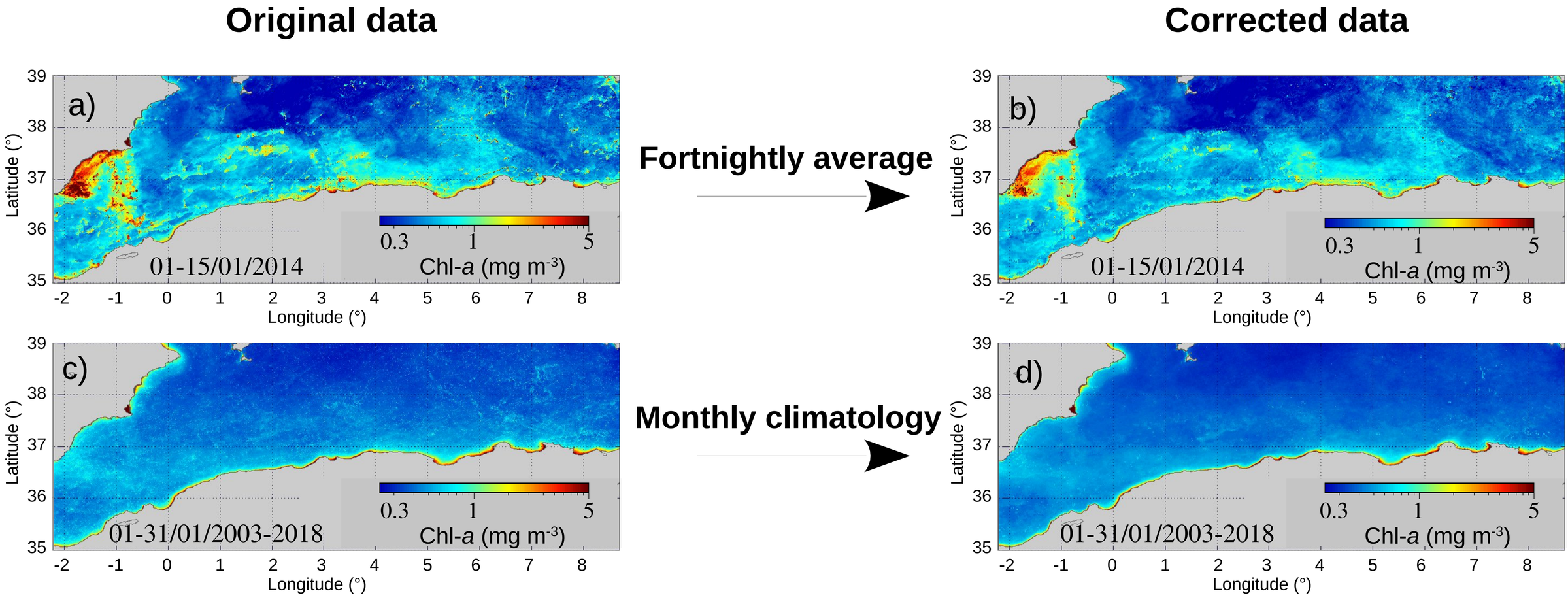
Original data
Corrected data
Fortnightly average
Monthly climatology
a)
b)
c)
d)
01-15/01/2014
01-31/01/2003-2018
Chl-a (mg m-3)
0.3
1
5
Latitude (°)
Longitude (°)
39
38
37
36
35
-2
-1
0
1
2
3
4
5
6
7
8

Chl-*a* (mg m^{-3})

0.5 1.0 1.5 2.0

a)

MODIS Level-3 (4 Km)

b)

MODIS Level-2 Corrected (1 Km)

Distance (Km)

120 100 80 60 40 20 0

A S O N D J F M A M J J

c)

d)

Distance (km)

10 8 6 4 2 0

e)

f)

Chl-a (mg m^{-3})

0 1 2

0 2 4 6 8 10

Distance from coast (Km)

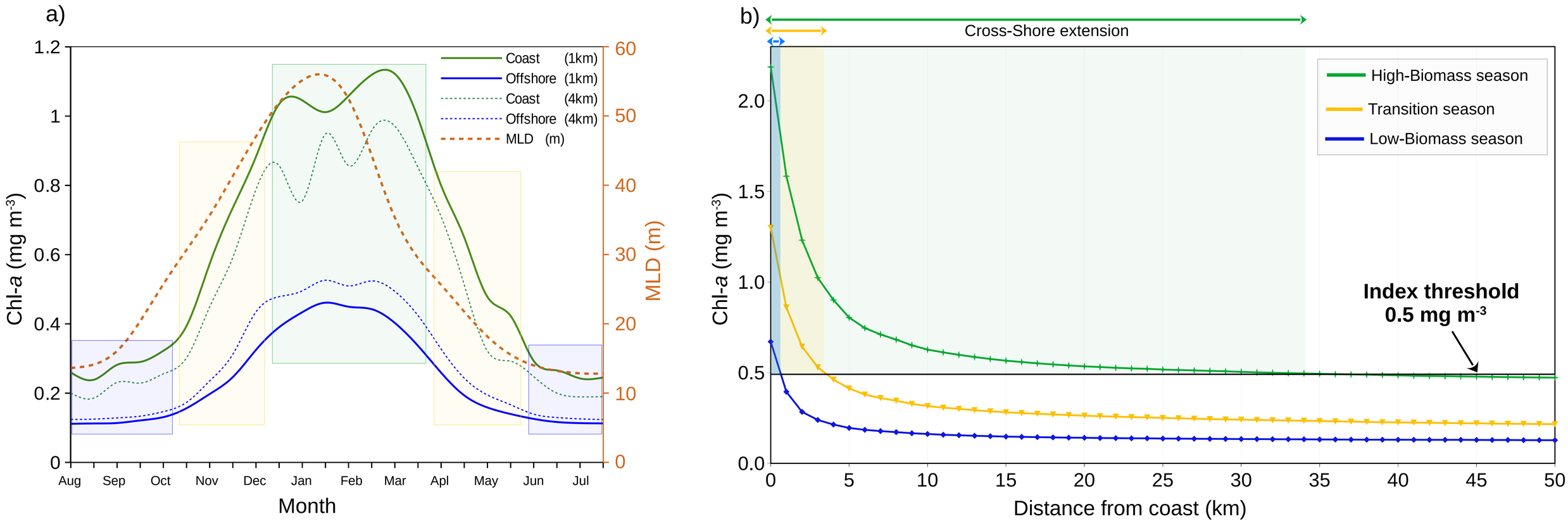
a)
Chl-a (mg m-3)
MLD (m)
Month
Aug
Sep
Oct
Nov
Dec
Jan
Feb
Mar
Apl
May
Jun
Jul
Coast (1km)
Offshore (1km)
Coast (4km)
Offshore (4km)
MLD (m)
b)
Cross-Shore extension
Chl-a (mg m-3)
Distance from coast (km)
High-Biomass season
Transition season
Low-Biomass season
Index threshold
0.5 mg m-3

a)

b)

c)

d)

0 20 40 60 80

$Dist_{0.5mg}$ (km)

0 0.5 1 1.5 2 2.5

Chl-*a* (mg m^{-3})

0 10 20 30 40 50

I_B (g m^{-2})

Longitude (°)

8
6
4
2
0
-2

Annaba bay
7.5°E
Skikda bay
Jijel bay
Bejaïa Gulf
4.5°E
Zemmouri bay
Algiers bay
Bou-Ismaïl bay
Algerian basin
$Dist^{max}_{0.5\,mg}$
10 km
Arzew Gulf
Oran Bay
1°W
N

39 °N 38 °N 37 °N 36 °N

x

=

A S O N D J F M A M J J

a)

b)

c)

d)

0 0.5 1 1.5 2 2.5

Chl-*a* coastal (mg m^{-3})

0 0.2 0.4 0.6 0.8 1

Chl-*a* offshore (mg m^{-3})

0 10 20 30 40 50

I_B coastal (g m^{-2})

0 10 20 30 40 50

I_B offshore (g m^{-2})

Longitude (°)

8 6 4 2 0 -2

A S O N D J F M A M J J

MLD
Biomass index
TKE

a) 1°W

b) 4.5°E

c) 7.5°E

Integrated biomass index (g m^{-2})

Mixed Layer Depth (m)

Total Kinetic Energy (m^2 s^{-2})

0
10
20
30
40
50

0
20
40
60
80

0.01
0.03
0.05

A S O N D J F M A M J J

Month

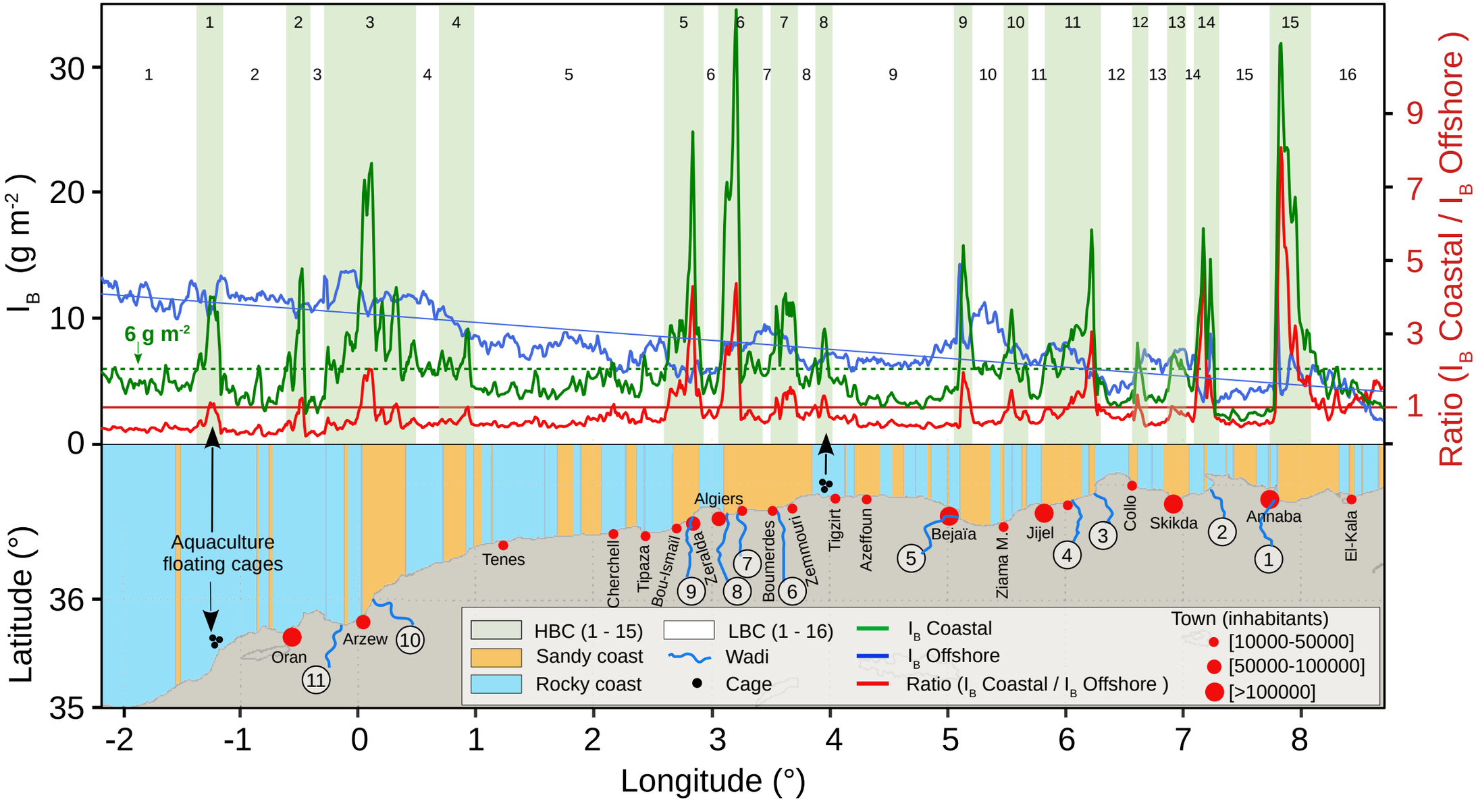
1
2
3
4
5
6
7
8
9
10
11
12
13
14
15
16
30
20
10
0
I_B (g m^{-2})
6 g m^{-2}
9
7
5
3
1
Ratio (I_B Coastal / I_B Offshore)
Aquaculture floating cages
Oran
Arzew
Tenes
Cherchell
Tipaza
Bou-Ismail
Algiers
Zeralda
Boumerdes
Zemmouri
Tigzirt
Azeffoun
Bejaïa
Ziama M.
Jijel
Collo
Skikda
Annaba
El-Kala
Latitude (°)
36
35
-2
-1
0
1
2
3
4
5
6
7
8
Longitude (°)
HBC (1 - 15)
Sandy coast
Rocky coast
LBC (1 - 16)
Wadi
Cage
I_B Coastal
I_B Offshore
Ratio (I_B Coastal / I_B Offshore)
Town (inhabitants)
[10000-50000]
[50000-100000]
[>100000]

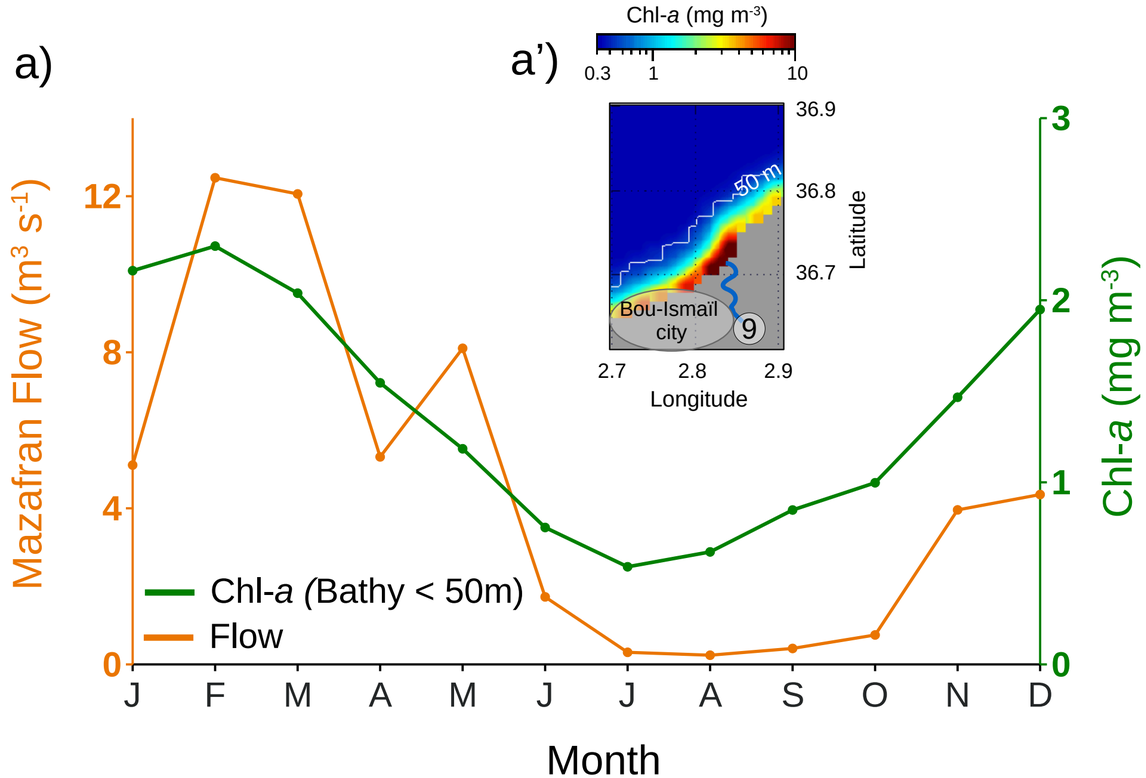
a)
a')
Chl-a (mg m-3)
0.3
1
10
36.9
36.8
36.7
Latitude
50 m
Bou-Ismaïl
city
9
2.7
2.8
2.9
Longitude
Mazafran Flow (m3 s-1)
12
8
4
0
3
2
1
0
Chl-a (mg m-3)
Chl-a (Bathy < 50m)
Flow
J
F
M
A
M
J
J
A
S
O
N
D
Month

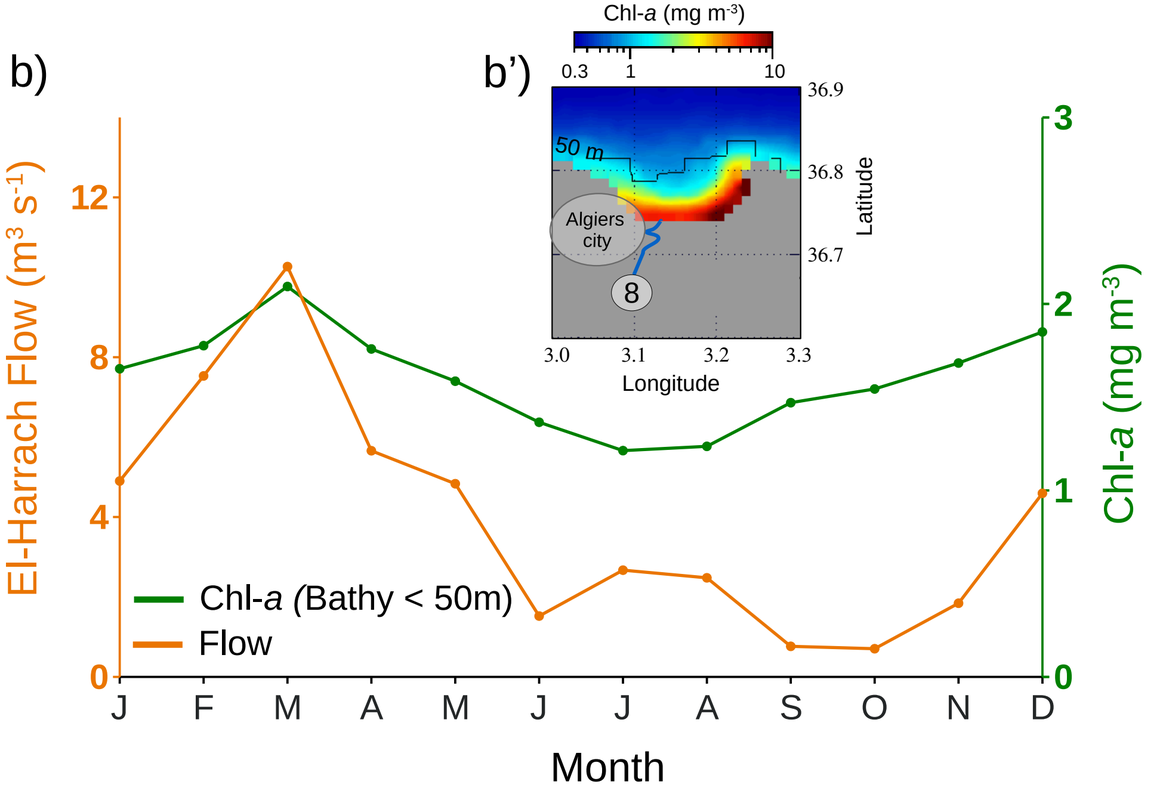
b)
b')
Chl-a (mg m-3)
0.3
1
10
36.9
36.8
36.7
Latitude
50 m
Algiers
city
8
3.0
3.1
3.2
3.3
Longitude
El-Harrach Flow (m3 s-1)
12
8
4
0
3
2
1
0
Chl-a (mg m-3)
Chl-a (Bathy < 50m)
Flow
J
F
M
A
M
J
J
A
S
O
N
D
Month

Season	I_B Coastal (g m^{-2})		I_B Offshore (g m^{-2})		I_B Coastal / I_B Offshore	
	summer	*winter*	*summer*	*winter*	*Jan & Feb*	*Dec & Mar*
LBC	0.7	10.1	0.317	23.2	***0.64***	***2.57***
HBC	2.9	18.2	0.626	24.8	***0.73***	**4.14**
HBC / LBC (%)	***+305%***	***+80%***	***+97%***	***+7%***		

LBC n°	1	2	3	4	5	6	7	8	9	10	11	12	13	14	15	16
Chl-*a* (mg m^{-3})	0.67	0.50	0.46	0.76	0.63	0.72	0.69	0.77	0.55	0.76	0.65	0.54	0.54	0.60	0.37	0.61
I_B (g m^{-2})	4.9	4.0	3.2	5.7	4.6	4.7	5.6	5.3	3.8	5.9	4.8	3.7	3.8	4.5	2.4	4.2
City size [0-3]					●				●							●
Coast-type	R	R	R	R	R	R	S	S	R	S	R	R	R	R	S	S
Wadi presence																
Bay (or gulf)										B						

HBC n°	1	2	3	4	5	6	7	8	9	10	11	12	13	14	15
Chl-*a* (mg m^{-3})	0.71	0.75	1.00	0.81	1.11	1.47	1.14	1.11	1.12	0.84	1.04	0.63	0.85	1.22	1.59
I_B (g m^{-2})	8.6	8.0	9.7	6.5	10.0	13.2	9.4	8.7	11.6	7.9	8.6	7.2	6.5	11.5	14.4
City size [0-3]		●	●		●	●	●		●	●	●	●	●		●
Coast-type	R, ●	R	S	S	S	S	S	R, ●	S	R	S	S	S	R	S
Wadi presence			≈		≈	≈	≈		≈					≈	≈
Bay (or gulf)		B	B		B	B	B		B	B	B		B	B	B

Model	Season	Response variables	Explanatory variables	p-value	Model %
m1	All seasons	[HBC ; LBC]	Coast type	-	67%
			Bay	-	
			Wadi	-	
			City	**	
m2	Winter	Chl-*a* ≥ 1.5	Coast type	-	79%
			Bay	-	
			Wadi	***	
			City	*	
m3		I_B ≥ 13	Coast type	-	77%
			Bay	**	
			Wadi	-	
			City	**	
m4	Summer	Chl-*a* ≥ 0.5	Coast type	-	57%
			Bay	-	
			Wadi	*	
			City	-	
m5		I_B ≥ 2.4	Coast type	-	78%
			Bay	*	
			Wadi	*	
			City	-	

Statistical signification of p-value (correlation is significant with p-value < 0.05 (5%)):

*** < 0.1 % ; ** < 1% ; * < 5% ; 5% < . < 10% ; - > 10%